

QUANTUM MANY-BODY FRAMEWORK

This chapter is dedicated to introducing the necessary tools needed to perform realistic material calculations using DMFT or D Γ A. We start with the most central objects - the Green's functions - and subsequently assemble a complete framework which enables us to calculate a number of physical properties, e.g. the susceptibility, optical conductivity, superconductivity, pseudogap formation and more, that stem from the correlated interplay between electrons or holes.

1.1 One-particle Green's functions

Green's functions are fundamental tools in many-body physics, used to study the properties and behavior of interacting quantum systems. These mathematical objects encode information about the propagation of particles or excitations within a system and serve as the cornerstone for analyzing both equilibrium and nonequilibrium states. In the many-body regime, Green's functions extend beyond single-particle descriptions to include complex interactions among multiple particles. They provide insights into phenomena such as quasiparticle lifetimes, collective excitations and response functions. Specifically, one- and two-particle Green's functions describe the propagation of a single particle and the correlated motion of particle pairs, respectively. Alongside of the mathematical description of Green's function-based expressions, we also provide a pictorial description of the equations using Feynman diagrams. These Feynman diagrams allow us to easily describe interaction processes visually. Lines and vertices within the diagrams indicate particle propagators and interaction vertices, respectively. External legs will be colored gray while inner legs and interaction lines will be colored black.

In condensed matter physics, we are only interested in finite-temperature effects. Hence it is practical to use the so-called Matsubara formalism[T. Matsubara. "A new approach to quantum-statistical mechanics"] in imaginary time by performing a Wick rotation $t \rightarrow -i\tau$ [G. C. Wick. "Properties of Bethe-Salpeter Wave Functions"]

Furthermore, most many-body quantities described in the following are n -point (correlation) functions^[1]. These functions typically include a subset of the following parameters for each external leg: (Matsubara) frequency (ν), spin index (σ), orbital index (o), lattice position (\mathbf{R}), momentum (\mathbf{k}) or imaginary time (τ). This introduces a huge amount of parameters appended to a variable and can be very cumbersome to read through if explicitly written down. Therefore, to increase readability, we follow Ref. [N. E. Bickers and D. J. Scalapino. "Conserving approximations ..."] and group all indices that are not explicitly written down into a compound index, e.g. $i = \{o_i, \sigma_i, \mathbf{R}_i\}$. If an equation containing spatial or momentum-dependent quantities is written down with a compound index, it applies equally in both real and Fourier space. Furthermore, summing over these compound indices means summing over all individual components they include, with a normalization of $\frac{1}{\beta}$ for frequency sums and $\frac{1}{N_k}$ for momentum sums, where $\beta = \frac{1}{k_B T}$ is the inverse temperature and N_k is the total number of reciprocal lattice points.

After this short introduction, let us dive in by defining the most central quantity, the two-point (one-

^[1]Here, n denotes the number of "connection points" of the corresponding Feynman diagram.

particle) Green's function, in a system in thermal equilibrium as

$$G_{12}^k = -\langle \mathcal{T} [\hat{c}_{k1} \hat{c}_{k2}^\dagger] \rangle, \quad (1.1)$$

where \hat{c}_{ki} (\hat{c}_{ki}^\dagger) are fermionic annihilation (creation) operators which annihilate (create) an electron with parameters $i = \{\sigma_i, o_i, \tau_i\}$ and momentum \mathbf{k} in the system. $\langle \cdot \rangle = \frac{1}{Z} \text{Tr} \{e^{-\beta \hat{\mathcal{H}}} \cdot\}$ with $Z = \text{Tr} \{e^{-\beta \hat{\mathcal{H}}}\}$ describes the thermal expectation value. Note, that the time evolution operator $e^{i\hat{\mathcal{H}}t} = e^{\hat{\mathcal{H}}\tau}$ is real after performing the Wick rotation to imaginary time and the Boltzmann weight $e^{\beta \hat{\mathcal{H}}}$ describes nothing more than an additional evolution in imaginary time. Lastly, $\mathcal{T}[\cdot]$ is the imaginary time ordering operator, where

$$\mathcal{T} [\hat{c}_1^{(\dagger)}(\tau_1) \hat{c}_2^{(\dagger)}(\tau_2)] = \Theta(\tau_1 - \tau_2) \hat{c}_1^{(\dagger)}(\tau_1) \hat{c}_2^{(\dagger)}(\tau_2) - \Theta(\tau_2 - \tau_1) \hat{c}_2^{(\dagger)}(\tau_2) \hat{c}_1^{(\dagger)}(\tau_1). \quad (1.2)$$

The Green's function measures the probability amplitude of a propagation process and reads as a Feynman diagram

$$G_{12} = \begin{array}{c} 1 \\ \bullet \end{array} \longrightarrow \begin{array}{c} 2 \\ \bullet \end{array}.$$

FIGURE 1.1 – Diagrammatic representation of the one-particle Green's function G_{12} . The electron is annihilated at 1, propagates in imaginary time from τ_1 to τ_2 and is created at 2.

In homogeneous systems, e.g., infinite or translationally invariant systems, the Green's function inherits the system's properties and becomes invariant under spatial translations. This means that $G_{12}(\mathbf{R}_1, \mathbf{R}_2) = G_{12}(\mathbf{R}_1 - \mathbf{R}_2, \mathbf{0}) = G_{12}(\mathbf{R})$. In Fourier space, this means that the Green's function is also only dependent on a single momentum parameter, $G_{12}(\mathbf{k}_1, \mathbf{k}_2) = G_{12}(\mathbf{k}_1 - \mathbf{k}_2, \mathbf{0}) = G_{12}(\mathbf{k})$. Furthermore, if the system is stationary, i.e., the Hamiltonian is not explicitly dependent on imaginary time, then $G_{12}(\tau_1, \tau_2) = G_{12}(\tau_1 - \tau_2, 0) = G_{12}(\tau)$. In absence of spin-orbit coupling, the spins at 1 and 2 need to be equal and therefore G_{12} only depends on a single spin component. Additionally, the *fermionic* Green's function can be shown to be anti-periodic in imaginary time with a period of β ^[2],

$$G_{12}(\tau) = -G_{12}(\beta - \tau) \quad \text{for } \tau > 0 \text{ and} \quad (1.3a)$$

$$G_{12}(\tau) = -G_{12}(\beta + \tau) \quad \text{for } \tau < 0. \quad (1.3b)$$

This anti-periodicity in time leads to the Fourier transform to be defined over a discrete set of imaginary frequencies, the so-called Matsubara frequencies, which for fermionic quantities are given by $\nu_n = (2n + 1)\frac{\pi}{\beta}$. In contrast, *bosonic* Green's functions are periodic in imaginary time with period β and therefore the Fourier transform includes the set of bosonic Matsubara frequencies $\omega_n = (2n)\frac{\pi}{\beta}$. In the following, we will always denote fermionic Matsubara frequencies with ν_n and bosonic ones with ω_n . The fermionic- and bosonic-like Fourier transforms of $G_{12}(\tau)$ become, respectively,

$$G_{12}(i\nu_n) = \int_0^\beta d\tau G_{12}(\tau) e^{i\nu_n \tau} \quad \text{and} \quad G_{12}(i\omega_n) = \int_0^\beta d\tau G_{12}(\tau) e^{i\omega_n \tau} \quad (1.4)$$

and only require the knowledge of Green's functions for positive imaginary times τ . The inverse Fourier transforms are given by

$$G_{12}(\tau) = \frac{1}{\beta} \sum_n G_{12}(i\nu_n) e^{-i\nu_n \tau} \quad \text{and} \quad G_{12}(\tau) = \frac{1}{\beta} \sum_n G_{12}(i\omega_n) e^{-i\omega_n \tau}. \quad (1.5)$$

^[2]This originates from the Boltzmann term $e^{\beta \hat{\mathcal{H}}}$ in the thermal expectation value and restricts the imaginary time domain to $\tau \in [-\beta, \beta)$.

If we perform a spectral representation of the fermionic Green's function in Eq. (1.1) and calculate the discrete Fourier transform, we find that

$$G_{12}(i\nu_n) = \frac{1}{Z} \sum_{mn} \left(e^{-\beta E_n} + e^{-\beta E_m} \right) \frac{\langle n | \hat{c}_1 | m \rangle \langle m | \hat{c}_2^\dagger | n \rangle}{i\nu - (E_m - E_n)}. \quad (1.6)$$

If we take $1 \equiv 2$, which corresponds to the *local* Green's function, we can introduce the spectral function

$$A_1(\nu) = \frac{1}{Z} \sum_{mn} e^{-\beta E_n} \left(1 + e^{-\beta \nu} \right) |\langle n | \hat{c}_1 | m \rangle|^2 \delta(\nu - E_m - E_n), \quad (1.7)$$

where

$$G_1(i\nu_n) = \int_{\mathbb{R}} d\nu \frac{A_1(\nu)}{i\nu_n - \nu}. \quad (1.8)$$

The spectral function $A_1(\nu)$ is the probability of adding or removing a particle with momentum \mathbf{k}_1 with spin σ_1 from the system. For that reason, $A_1(\nu)$ is coined the single-particle local density of states. Furthermore, since it represents a probability distribution, the integral over all energies of $A_1(\nu)$ is equal to 1. It is directly measurable using techniques like angle-resolved photoemission spectroscopy (ARPES) [**Quasiparticle spectral function, full momentum and energy resolved**], which probes electronic states in the material and reveals electronic structure properties, such as band gaps and quasiparticle dispersions. The peaks in $A_1(\nu)$ correspond to quasiparticle states, with their position indicating the energy of these states and their width related to the lifetime or decay rate of the quasiparticles. A narrow peak indicates a well-defined quasiparticle with a long lifetime and weak decay rate, while a broad peak suggests the contrary. The spectral function is a key quantity in many-body theory as it connects real-world experimental results to the Green's function formalism, as is shown in Refs. [**Quasiparticle spectral function, full momentum and energy resolved**] and the following. By performing analytic continuation in the upper complex plane ($i\nu \rightarrow \nu + i0^+$), one can define the retarded Green's function as

$$G_1^R(\nu) = \int_{\mathbb{R}} d\nu' \frac{A_1(\nu')}{\nu - \nu' + i0^+}, \quad (1.9)$$

from where one obtains through the Kramers-Kronig relations

$$A_1(\nu) = -\frac{1}{\pi} \Im G_1^R(\nu). \quad (1.10)$$

Thus, the spectral function is directly coupled to the imaginary part of the retarded Green's function, connecting many-body theory with physical experiments.

As an example, which will prove itself useful for the future, let us consider non-interacting electrons in a system with translational symmetry that are described by the (Wannier-) Hamiltonian

$$\hat{\mathcal{H}}_0 = \sum_{\mathbf{k};12} \varepsilon_{12}(\mathbf{k}) \hat{c}_{\mathbf{k};1}^\dagger \hat{c}_{\mathbf{k};2}, \quad (1.11)$$

where $\varepsilon_{12}(\mathbf{k}) = -\sum_{\mathbf{R};12} t_{12}(\mathbf{R}) e^{i\mathbf{k}\mathbf{R}}$ is the momentum dispersion of the band and is measured with respect to the chemical potential μ . In this case, it is easy to show, that

$$G_{0,12}(\nu, \mathbf{k}) = [i\nu\delta_{12} - \varepsilon_{12}(\mathbf{k})]^{-1}. \quad (1.12)$$

For the one-particle spectral function, we find in this case

$$A_{12}(\varepsilon, \mathbf{k}) = \delta(\varepsilon - \varepsilon_{\mathbf{k},12}), \quad (1.13)$$

corresponding to stable quasiparticles, due to zero width of the quasiparticle peak of $A_{12}(\varepsilon, \mathbf{k})$.

The direct computation of the Green's function as expressed in Eq. (1.1) generally incurs an exponential increase in cost with lattice size for interacting models. As a result, it is common practice to begin with the noninteracting case and construct a perturbative expansion in terms of the interaction around it. In this context, we will start with the non-interacting case described above. This perturbation expansion will not be derived in detail in this thesis, as there are many wonderful resources that explain it very thoroughly [Abrikosov, Nolting], thus we will only sketch it here. In essence, the expansion is constructed using the so-called S-matrix and employs strategies such as the Wick contraction [Wick, evaluation of collision matrix and Notes on wick's theorem] and the linked cluster theorem [linked cluster chapter in book]. The expansion begins by identifying the most general interaction part of the Hamiltonian of Eq. (??),

$$\hat{\mathcal{H}}_I = \frac{1}{2} \sum_{1234} U_{1234} \hat{c}_1^\dagger \hat{c}_3^\dagger \hat{c}_4 \hat{c}_2. \quad (1.14)$$

The expansion of the Green's function then reads

$$G_{12}(\tau) = -\frac{1}{\langle S(\beta) \rangle_0} \sum_{n=0}^{\infty} \frac{(-1)^n}{n!} \int_0^\beta d\tau_1 \cdots \int_0^\beta d\tau_n \langle \mathcal{T} [\hat{c}_1 \hat{c}_2^\dagger \hat{\mathcal{H}}_I(\tau_1) \cdots \hat{\mathcal{H}}_I(\tau_n)] \rangle_0, \quad (1.15)$$

where $S(\beta)$ is the abovementioned S-matrix and $\langle \cdot \rangle_0$ is the thermal expectation value in terms of the non-interacting Hamiltonian $\hat{\mathcal{H}}_0$. In Feynman diagram jargon, this contains all diagrams that are possible, also disconnected ones^[3]. The linked cluster theorem allows us to get rid of those disconnected contributions by effectively canceling with the $\frac{1}{\langle S(\beta) \rangle_0}$ term in front. This results in

$$G_{12}(\tau) = -\sum_{n=0}^{\infty} \frac{(-1)^n}{n!} \int_0^\beta d\tau_1 \cdots \int_0^\beta d\tau_n \langle \mathcal{T} [\hat{c}_1 \hat{c}_2^\dagger \hat{\mathcal{H}}_I(\tau_1) \cdots \hat{\mathcal{H}}_I(\tau_n)] \rangle_0^{\text{conn}}, \quad (1.16)$$

where $\langle \cdot \rangle_0^{\text{conn}}$ now indicates that we only consider connected diagrams in the expansion. We can transform this into a diagrammatic representation by applying Wick contractions, which allow us to collect pairs of creation and annihilation operators to form independent expectation values. In the case of the $n = 1$ term in the perturbation expansion of the Green's function,

$$\begin{aligned} G_{1,12}(\tau) = \sum_{abcd} \int_0^\beta d\tau_1 U_{abcd} \Big[& -\langle \mathcal{T} [\hat{c}_1(\tau) \hat{c}_a^\dagger(\tau_1)] \rangle_0 \langle \mathcal{T} [\hat{c}_d(\tau_1) \hat{c}_c^\dagger(\tau_1)] \rangle_0 \langle \mathcal{T} [\hat{c}_b(\tau_1) \hat{c}_2^\dagger(0)] \rangle_0 \\ & + \langle \mathcal{T} [\hat{c}_1(\tau) \hat{c}_a^\dagger(\tau_1)] \rangle_0 \langle \mathcal{T} [\hat{c}_b(\tau_1) \hat{c}_c^\dagger(\tau_1)] \rangle_0 \langle \mathcal{T} [\hat{c}_d(\tau_1) \hat{c}_2^\dagger(0)] \rangle_0 \Big]. \end{aligned} \quad (1.17)$$

The remaining expectation values are nothing more than minus the non-interacting Green's function of Eq. (1.12). Written in Feynman diagrams, the first relevant perturbation expansion term is shown in Fig. 1.2.

^[3]Disconnected means, that the term includes a diagram that consists of two separate, disconnected diagrams.

$$G_{1;12}(\tau) = \frac{1}{\tau} \rightarrow \frac{a}{\tau_1} b \rightarrow \frac{2}{0} + \frac{1}{\tau} \rightarrow \frac{a}{\tau_1} b \rightarrow \frac{c}{\tau_1} d \rightarrow \frac{1}{0}$$

FIGURE 1.2 – First order diagrams for the single-particle Green’s function. The corresponding diagrams are coined the Hartree- and the Fock-term, respectively. As the name suggests, taking only these two diagrams as the whole perturbation expansion leads to the Hartree-Fock approximation, formulated as a diagrammatic theory.

1.2 Self-energy

The one-particle Green’s function perturbative expansion is already much simplified in the graphical portrayal. However, the number of diagrams increases exponentially with order n ^[4]. Therefore, the Feynman diagram approach would be of little practical use if the only way to progress was to calculate each diagram one at a time. However, in reality the technique is actually quite useful, since it hints on how to sum up the perturbative series. Let us talk about how it applies to Green’s function for single particles. First, let us define another compound index which will further levitate readability. We will set $k = \{\nu, \mathbf{k}\}$ and $q = \{\omega, \mathbf{q}\}$ as a compound index including momentum and frequency in one index for fermionic (k) and bosonic (q) frequencies and momenta. Note, that if we write ν instead of k , we refer to the *local* part of the quantity with no momentum dependence instead of the *non-local* part. Diagrams in general can be split up into two classes: (i) diagrams that, by cutting a single internal Green’s function line, transform in two lower-order diagrams, which are called one-particle reducible and (ii) diagrams that are not one-particle reducible, which are called one-particle irreducible (1PI). Let us define as the one-particle self-energy Σ_{12}^k the sum of all irreducible diagrams without external legs. For example, the black part of the diagrams in Fig. 1.2 corresponds to the first-order diagrams of the self-energy. It is then straightforward to rewrite Eq. (1.16) in terms of the self-energy, yielding

$$G_{12}^k = G_{0,12}^k + \sum_{ab} G_{0,1a}^k \Sigma_{ab}^k G_{b2}^k, \quad (1.18)$$

which results in - when taking Eq. (1.12) as the noninteracting Green’s function and inverting in frequency and momentum space - a way to express the full (interacting) single-particle Green’s function in terms of the self-energy

$$G_{12}^k = \left[i\nu_n \delta_{12} - \varepsilon_{12}(\mathbf{k}) - \Sigma_{12}^k \right]^{-1}. \quad (1.19)$$

Eq. (1.18) is commonly known as the Dyson equation [**dyson eq**] for the single-particle Green’s function and for completeness, its diagrammatic representation can be found in Fig. 1.3. It is a geometric series, where each term in the sum subsequently adds irreducible diagrams that are pieced together by non-interacting Green’s functions to generate all possible diagrams. The self-energy can be obtained by simply inverting Eq. (1.18),

$$\Sigma_{12}^k = (G_{0,12}^k)^{-1} - (G_{12}^k)^{-1}. \quad (1.20)$$

Thus, perturbation theory can be done in two distinct ways: the simpler approach is to determine the Green’s function directly, for example, up to order n , where the second method is to compute

^[4]For $n = 2$ there exist 10 diagrams, for $n = 7$ the number of diagrams is well over a million.

$$G_{12}^k = \text{thick line from 1 to 2 with } k \text{ below} = \text{thin line from 1 to } a \text{ with } k \text{ below} \circlearrowleft \Sigma_{ab}^k \circlearrowright \text{thin line from } b \text{ to } 2 \text{ with } k \text{ below}$$

FIGURE 1.3 – Diagrammatic representation of Eq. (1.18). The full Green's function G_{12}^k is drawn as a thick black line.

the self-energy up to order n and insert its expression in the Dyson equation Eq. (1.18). This gives an approximate Green's function containing each order of perturbation theory with only a subset of all possible diagrams. As a result, Eq. (1.18) represents a way to sum up perturbation theory and is actually more relevant from a physical standpoint. Indeed, many methods leverage the usefulness of this approach, for example the dynamical mean-field theory or the dynamical vertex approximation, as we will see later.

Let us add some physical background to the self-energy in the following. Σ represents the effects of the interaction on the single electron propagators. The real and imaginary part of the self-energy have significant impact on the physical properties of the system. The real part of the self-energy contributes to an energy shift of the electronic states of the single-particle energy levels $\varepsilon(\mathbf{k})$ due to interactions. In contrast, the imaginary part of the self-energy is related to the decay or lifetime of quasiparticles and introduces a spectral broadening or damping of the electronic states, indicating how long an excitation or quasiparticle persists before interacting with other excitations or scattering events. A larger imaginary part implies a shorter lifetime and stronger interactions. The first order derivative in frequency, $\frac{\partial \Sigma^k}{\partial \nu}$, contributes to an effective renormalization of the bare electron mass. It also leads to a redistribution of spectral weight in the one-particle spectral function, which provides information about the distribution of energy levels available for excitations. A broader spectral function, whose broadening is controlled by the imaginary part of the self-energy, typically indicates stronger interactions and a more correlated system.

1.3 Two-particle Green's functions

In analogy to the one-particle Green's function, the two-particle Green's function describes the amplitude of the propagation of two particles, two holes or a particle and a hole. A similar expression to Eq. (1.1) can be formulated for the two-particle Green's function

$$G_{1234}^{\text{qkk}'} = - \left\langle \mathcal{T} \left[\hat{c}_{\mathbf{k};1} \hat{c}_{\mathbf{k}-\mathbf{q};2}^\dagger \hat{c}_{\mathbf{k}'-\mathbf{q};3} \hat{c}_{\mathbf{k}';4}^\dagger \right] \right\rangle. \quad (1.21)$$

It describes two particles, two holes or a particle and a hole being inserted in the system at times τ_2 and τ_4 , propagating in the system until they are removed again at τ_1 and τ_3 , respectively. Assuming a stationary Hamiltonian that satisfies time-translation invariance, it is possible to eliminate one imaginary time variable by setting it zero. Then, the Green's function only depends on three time variables and through Fourier transform, also only depends on three frequency and momentum variables. Furthermore, similar to the case for the one-particle Green's function, the absence of spin-orbit coupling reduces the number of spin degrees of freedom

$$G_{\sigma\sigma';1234}^{\text{qkk}'} = G_{\sigma\sigma'\sigma';1234}^{\text{qkk}'} \quad \text{and} \quad (1.22a)$$

$$G_{\sigma\sigma';1234}^{\text{qkk}'} = G_{\sigma\sigma'\sigma';1234}^{\text{qkk}'} \quad (1.22b)$$

In this case, the total incoming and outgoing spin must be equal and this puts a heavy constraint on the possible spin combinations,

$$\sigma_1 = \sigma_2 = \sigma_3 = \sigma_4, \quad (\sigma_1 = \sigma_2) \neq (\sigma_3 = \sigma_4) \quad \text{and} \quad (\sigma_1 = \sigma_4) \neq (\sigma_2 = \sigma_3), \quad (1.23)$$

totaling to only six unique spin combinations, each of which can be seen in Fig. 1.4. Furthermore, if

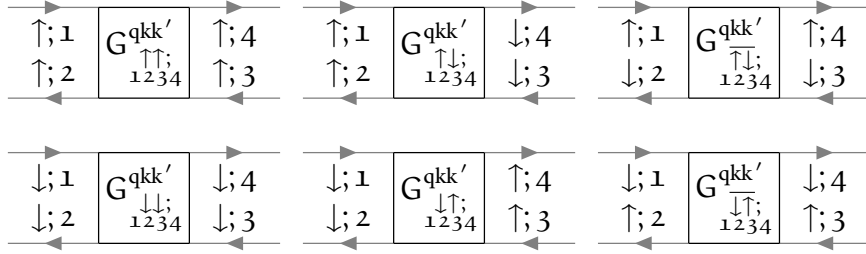


FIGURE 1.4 – In the case of absent spin-orbit coupling, these are the only non-vanishing spin combinations of the two-particle Green's function.

one describes quantities in the paramagnetic phase, where the system is SU(2)-symmetric, there are only two independent spin configurations,

$$G_{\sigma\sigma';1234}^{qkk'} = G_{(-\sigma)(-\sigma');1234}^{qkk'} = G_{\sigma'\sigma;1234}^{qkk'} \quad \text{and} \quad (1.24a)$$

$$G_{\sigma\sigma;1234}^{qkk'} = G_{\sigma(-\sigma);1234}^{qkk'} + G_{\sigma(-\sigma);1234}^{qkk'}. \quad (1.24b)$$

For these two spin combinations, the (d)ensity, (m)agnetic, (s)inglet and (t)riplet channel^[5] specified in the following are a particularly helpful choice of notation, as we shall see in the upcoming sections:

$$G_{d;1234}^{qkk'} = G_{\uparrow\uparrow;1234}^{qkk'} + G_{\uparrow\downarrow;1234}^{qkk'}, \quad (1.25a)$$

$$G_{m;1234}^{qkk'} = G_{\uparrow\uparrow;1234}^{qkk'} - G_{\uparrow\downarrow;1234}^{qkk'} = G_{\uparrow\downarrow;1234}^{qkk'}, \quad (1.25b)$$

$$G_{s;1234}^{qkk'} = G_{\uparrow\downarrow;1234}^{qkk'} - G_{\uparrow\downarrow;1234}^{qkk'} \quad \text{and} \quad (1.25c)$$

$$G_{t;1234}^{qkk'} = G_{\uparrow\downarrow;1234}^{qkk'} + G_{\uparrow\downarrow;1234}^{qkk'}. \quad (1.25d)$$

Besides the spin-symmetries discussed above, the Green's function also inherits other properties of the system, such as time-reversal symmetry, which manifests itself by

$$G_{1234}^{qkk'} = G_{4321}^{\bar{q}\bar{k}'\bar{k}}, \quad (1.26)$$

where $\bar{k} = \{\nu, -\mathbf{k}\}$ is the time-reversed compound momentum variable. Furthermore, the two-particle Green's function satisfies the crossing symmetry, which is a direct manifestation of Pauli's principle. Crossing symmetry refers to the antisymmetric property of the Green's function with respect to the exchange of the incoming and outgoing fermions

$$G_{\sigma\sigma';1234}^{qkk'} = -G_{\sigma'\sigma;3214}^{(k'-k)(k'-q)k'} \quad (1.27a)$$

$$= -G_{\sigma\sigma';1432}^{(k-k')k(k-q)} \quad (1.27b)$$

$$= G_{\sigma'\sigma;3412}^{(-q)(k'-q)(k-q)}. \quad (1.27c)$$

^[5] As we will see later, in $ph/\bar{p}h$ -notation, the Bethe-Salpeter equation will become diagonal for the d/m spin combination as well as for pp-notation in the s/t spin combination.

The symmetries Eq. (1.27a) - Eq. (1.27c) describe the frequency changes that occur by exchanging the positions of the gray fermion lines, leaving the vertex unchanged. The last line corresponds to a full swap of the incoming and outgoing particle labels. The crossing symmetry is visually shown in Fig. 1.5. Lastly, the Green's function also possesses symmetry with respect to complex conjugation,

$$\left(G_{\sigma\sigma';1234}^{qkk'}\right)^* = G_{\sigma'\sigma;4321}^{(-q)(-k)(-k')}. \quad (1.28)$$

At the beginning of the section it was stated that the (four-point) two-particle Green's function only

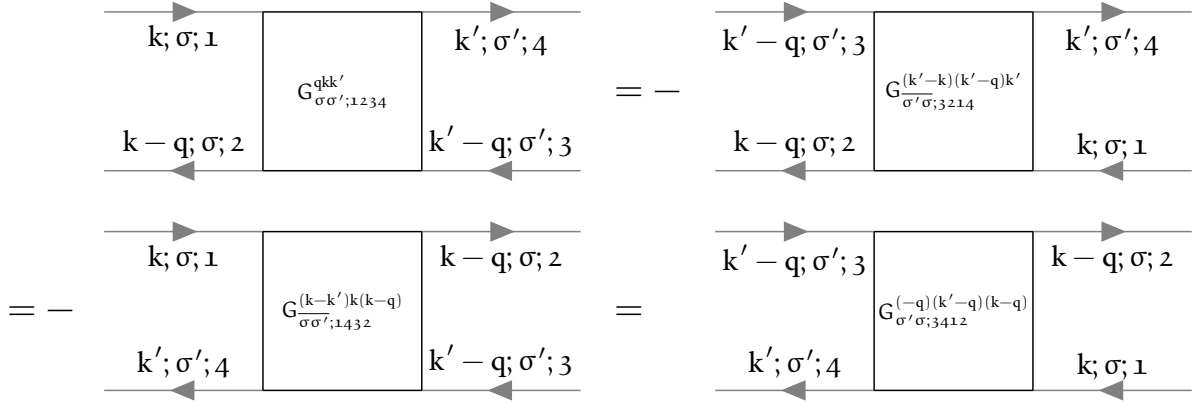


FIGURE 1.5 – Diagrammatic representation of the crossing symmetry relations in order of Eq. (1.27a) - Eq. (1.27c).

requires three frequency arguments to be fixed since the last one is automatically given by momentum conservation. There are three equivalent choices (coined channels) of independent frequencies (with ν, ν' being a fermionic and ω a bosonic Matsubara frequency)

$$\text{ph-notation: } \{\nu_1 = \nu, \quad \nu_2 = \nu - \omega, \quad \nu_3 = \nu' - \omega, \quad \nu_4 = \nu'\}, \quad (1.29a)$$

$$\overline{\text{ph-notation: } \{\nu_1 = \nu, \quad \nu_2 = \nu', \quad \nu_3 = \nu' - \omega, \quad \nu_4 = \nu - \omega\}} \quad \text{and} \quad (1.29b)$$

$$\text{pp-notation: } \{\nu_1 = \nu, \quad \nu_2 = \omega - \nu', \quad \nu_3 = \omega - \nu, \quad \nu_4 = \nu'\}. \quad (1.29c)$$

To show the effects of this frequency shift and how they affect the labels of the diagrams, we show the two-particle Green's function in the three notations of Eq. (1.29a) - Eq. (1.29c) in Fig. 1.6 below. Obviously, the choice of frequency convention should not have any impact on the physical content of the Green's function, hence it is possible to switch between these channels by applying channel-specific frequency shifts [**continuous qmc asympt**],

$$G_{\text{ph};1234}^{qkk'} = G_{\text{ph};1234}^{(k-k')k(k-q)}, \quad (1.30a)$$

$$G_{\text{ph};1234}^{qkk'} = G_{\text{ph};1234}^{(k-k')k(k-q)}, \quad (1.30b)$$

$$G_{\text{ph};1234}^{qkk'} = G_{\text{pp};1234}^{(k+k'-q)kk'} \quad \text{and} \quad (1.30c)$$

$$G_{\text{pp};1234}^{qkk'} = G_{\text{ph};1234}^{(k+k'-q)kk'}. \quad (1.30d)$$

Let us finally note that the two-particle Green's function represents all diagrams that are possible that involve two electrons, two holes or an electron and a hole. It can therefore be split into two parts: (i) a part, where the electrons do not interact with each other and propagate independently; and (ii) a part, where the electrons do interact with each other through an infinite number of processes. (ii) is

$$\begin{aligned}
G_{\text{ph};1234}^{\text{qkk}'} &= \begin{array}{|c|c|} \hline \begin{array}{c} \rightarrow k;1 \\ \leftarrow k-q;2 \end{array} & \begin{array}{c} \rightarrow k';4 \\ \leftarrow k'-q;3 \end{array} \\ \hline \end{array} G_{\text{ph};1234}^{\text{qkk}'} \\
G_{\overline{\text{ph}};1234}^{\text{qkk}'} &= \begin{array}{|c|c|} \hline \begin{array}{c} \rightarrow k;1 \\ \leftarrow k';2 \end{array} & \begin{array}{c} \rightarrow k-q;4 \\ \leftarrow k'-q;3 \end{array} \\ \hline \end{array} G_{\overline{\text{ph}};1234}^{\text{qkk}'} \\
G_{\text{pp};1234}^{\text{qkk}'} &= \begin{array}{|c|c|} \hline \begin{array}{c} \rightarrow k;1 \\ \leftarrow q-k';2 \end{array} & \begin{array}{c} \rightarrow k';4 \\ \leftarrow q-k;3 \end{array} \\ \hline \end{array} G_{\text{pp};1234}^{\text{qkk}'}
\end{aligned}$$

FIGURE 1.6 – Two-particle Green's functions in the different frequency notations of Eq. (1.29a) - Eq. (1.29c) expressed in Feynman diagrams. The frequency notation is encoded in an additional subscript, {ph, $\overline{\text{ph}}$, pp}.

commonly called the connected two-particle Green's function and can be mathematically formulated by

$$G_{\sigma\sigma';1234}^{\text{qkk}'} = G_{\sigma\sigma';1234}^{\text{conn;qkk}'} + \delta_{q0} G_{\sigma;12}^k G_{\sigma';34}^{k'} - \delta_{\sigma\sigma'} \delta_{kk'} G_{\sigma;14}^k G_{\sigma';32}^{k-q}. \quad (1.31)$$

Diagrammatically, the connected two-particle Green's function contains all diagrams, where two propagating electrons interact with each other. The first terms up to interaction order two are given in Fig. 1.7. The other terms in Eq. (1.31) are not that interesting, they merely describe the electrons

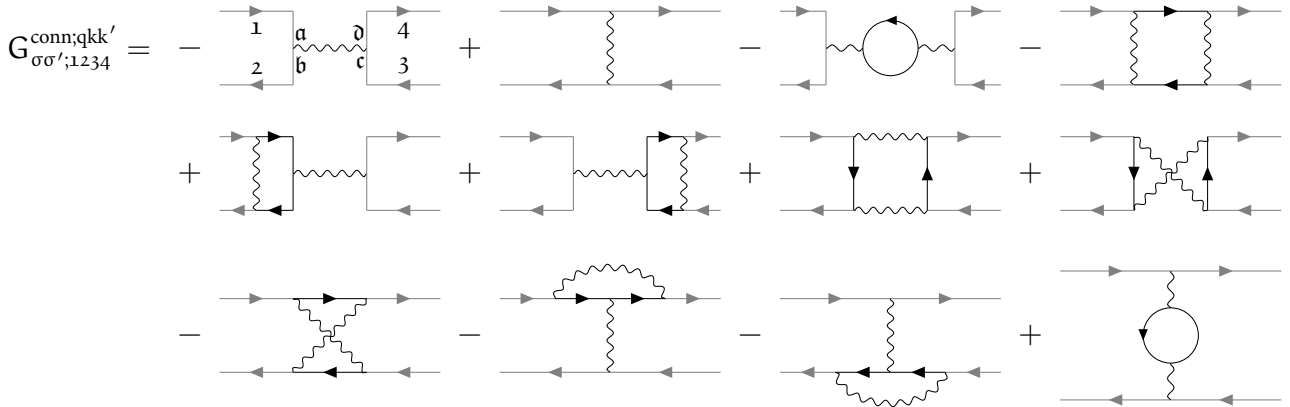


FIGURE 1.7 – Diagrammatic representation of the two-particle connected Green's function up to order two. It includes the possible interaction processes that occur between two propagating electrons. The particle labels are only written down for the first diagram, the other diagrams are labeled analogously.

propagating in the system without ever interacting with the other. However, we will still show the diagrammatic content of the second and third term of Eq. (1.31) in Fig. 1.8. The connected two-particle Green's function without the external legs is commonly called the full vertex F , where by convention

$$\delta_{q0} G_{\sigma;12}^k G_{\sigma';34}^{k'} - \delta_{\sigma\sigma'} \delta_{kk'} G_{\sigma;14}^k G_{\sigma';32}^{k-q} = \left[\begin{array}{c|c} 1 & 4 \\ \hline \delta_{q0} & \\ \hline 2 & 3 \end{array} \right] - \left[\begin{array}{c|c} 1 \rightarrow & 4 \\ \hline \delta_{\sigma\sigma'} \delta_{kk'} & \\ \hline 2 \leftarrow & 3 \end{array} \right]$$

FIGURE 1.8 – Disconnected part (second and third term on the right hand side of Eq. (1.31)) of the two-particle Green's function.

an additional minus sign is introduced,

$$G_{1234}^{\text{conn};qkk'} = -\frac{1}{\beta} \sum_{abcd} G_{1a}^k G_{b2}^{k-q} F_{abcd}^{qkk'} G_{3c}^{k'-q} G_{d4}^{k'}. \quad (1.32)$$

By the previous definition, the vertex function $F_{1234}^{qkk'}$ contains all diagrams that connect two incoming and two outgoing lines. All diagrams contained in the full vertex $F_{1234}^{qkk'}$ can be classified by their two-particle reducibility (2PR). A diagram is called two-particle reducible, if it can be split into two separate parts by cutting two internal Green's function lines. Furthermore, this classification is described by three channels, $\{\text{ph}, \overline{\text{ph}}, \text{pp}\}^{[6]}$, depending on which incoming and outgoing lines are being separated by this “cutting”-process. The ph-channel corresponds to those diagrams, where the sub-parts connect 12 and 34, for the $\overline{\text{ph}}$ -channel 14 and 23 and for the pp-channel 13 and 24 are connected. These reducible diagrams are categorized in $\Phi_{\text{ph};1234}^{qkk'}$, $\Phi_{\overline{\text{ph}};1234}^{qkk'}$ and $\Phi_{\text{pp};1234}^{qkk'}$, respectively. All diagrams that are not two-particle reducible are grouped together in the quantity $\Lambda_{1234}^{qkk'}$. This procedure is called the parquet decomposition and reads mathematically

$$F_{1234}^{qkk'} = \Lambda_{1234}^{qkk'} + \Phi_{\text{ph};1234}^{qkk'} + \Phi_{\overline{\text{ph}};1234}^{qkk'} + \Phi_{\text{pp};1234}^{qkk'}. \quad (1.33)$$

Another possibility is to split up the full vertex F in reducible and irreducible diagrams in a specific channel $r \in \{\text{ph}, \overline{\text{ph}}, \text{pp}\}$,

$$F_{1234}^{qkk'} = \Gamma_{r;1234}^{qkk'} + \Phi_{r;1234}^{qkk'}, \quad (1.34)$$

where $\Gamma_{r;1234}^{qkk'}$ is the irreducible vertex in channel r and $\Phi_{r;1234}^{qkk'}$ the corresponding reducible one. Note, that in channel r irreducible diagrams might still be reducible in another channel $r' \neq r$. For example, $\Gamma_{\text{ph};1234}^{qkk'}$ contains all fully irreducible diagrams, but also all diagrams which are reducible in channels $\overline{\text{ph}}$ and pp ,

$$\Gamma_{\text{ph};1234}^{qkk'} = \Lambda_{1234}^{qkk'} + \Phi_{\overline{\text{ph}};1234}^{qkk'} + \Phi_{\text{pp};1234}^{qkk'}. \quad (1.35)$$

This will be important later in Sec. 1.6, where we will discuss the Bethe-Salpeter equations. Furthermore, the following relations for the ph and $\overline{\text{ph}}$ channel for $\Gamma_{r;1234}^{qkk'}$ and $\Phi_{r;1234}^{qkk'}$ hold:

$$\Phi_{\text{ph};1234;\sigma\sigma'}^{qkk'} = -\Phi_{\text{ph};3214;\overline{\sigma'}\sigma}^{(k'-k)(k'-q)k'}, \quad (1.36a)$$

$$= -\Phi_{\text{ph};1432;\overline{\sigma'}\sigma}^{(k-k')k(k-q)}. \quad (1.36b)$$

^[6]The attentive reader remembers that there are also three (identically-named) frequency notations that were mentioned previously. The channel reducibility and frequency notation are - in general - detached. From now on, if only one channel argument r is given per vertex quantity, it means that the channel reducibility will belong to r and the frequency notation will be ph . Otherwise the channel reducibility and frequency notation will be denoted in the sub- and superscript of the variable, respectively. This will be relevant later when discussing the Bethe-Salpeter equation (BSE), see Sec. 1.6. The BSE is only diagonal in the bosonic transfer momentum and frequency q if the channel reducibility equals the frequency notation.

From this one can construct the density and magnetic contributions to $\Phi_{\text{ph};1234;\sigma\sigma'}^{\text{qkk}'}$ in terms of $\Phi_{\text{ph};1234;\sigma\sigma'}^{\text{qkk}'}$

$$\Phi_{\text{d;ph};1234}^{\text{qkk}'} = -\frac{1}{2}\Phi_{\text{d;ph};3214}^{(k'-k)(k'-q)k'} - \frac{3}{2}\Phi_{\text{m;ph};3214}^{(k'-k)(k'-q)k'} \quad (1.37a)$$

$$\Phi_{\text{m;ph};1234}^{\text{qkk}'} = -\frac{1}{2}\Phi_{\text{d;ph};3214}^{(k'-k)(k'-q)k'} + \frac{1}{2}\Phi_{\text{m;ph};3214}^{(k'-k)(k'-q)k'}. \quad (1.37b)$$

The relations Eq. (1.36) and Eq. (1.37) also apply to the full- and irreducible vertices $\Gamma_{\text{ph};1234;\sigma\sigma'}^{\text{qkk}'}$ and $\Gamma_{\text{ph};1234;\sigma\sigma'}^{\text{qkk}'}$ in a similar fashion. Note that there is no connection between the pp channel and the other two channels, hence it is not possible to transform the channel reducibility from either ph or $\overline{\text{ph}}$ to pp. The pp-channel fulfills a crossing symmetry on its own,

$$\Phi_{\text{pp};1234;\sigma\sigma'}^{\text{qkk}'} = -\Phi_{\text{pp};1432;\sigma\sigma'}^{(k-k')k(k-q)}. \quad (1.38)$$

As the next step, let us briefly introduce the concept of linear response and the central physical property describing the response of a system with respect to an external perturbation^[7], the susceptibility.

1.4 Susceptibility

Experimentally, it is not possible to directly extract information (just by “looking”) about the interactions between electrons in a system. Instead, in spectroscopic experiments, a perturbation is applied to the system and one measures the system’s response. In particular, one measures how expectation values $\langle \cdot \rangle$ of operators (take the multi-dimensional operator $\hat{O}_i(\tau)$ as an example) changes when an external field $h_j(\tau)$ is applied. In linear response theory, this response is — as the name suggests — taken to be linear in the perturbing field, requiring this field to be sufficiently small in order for this description to be a good approximation [**kappl susc**],

$$\langle \hat{O}_i(\tau) \rangle_{\mathbf{h}} - \langle \hat{O}_i(\tau) \rangle_{\mathbf{h}=0} = \int_0^\beta d\tau' \chi_{ij}(\tau - \tau') h_j(\tau') + \mathcal{O}(\mathbf{h}^2), \quad (1.39)$$

where $\chi_{ij}(\tau - \tau')$ is coined physical susceptibility and does not depend on the field $h_j(\tau)$. $\chi(\tau - \tau')$ fulfills the Kramers-Kronig relations, is causal ($\chi_{ij}(\tau - \tau') = \Theta(\tau - \tau')\chi_{ij}(\tau - \tau')$) and is finite ($\forall \tau, \tau' : \exists C \in \mathbb{R} : |\chi_{ij}(\tau - \tau')| < C$). The susceptibility can be computed straightforwardly by taking the functional derivative of $\hat{O}_i(\tau)$ with respect to the field $h_j(\tau)$,

$$\chi_{ij}(\tau - \tau') = \left. \frac{\delta \langle \hat{O}_i(\tau') \rangle}{\delta h_j(\tau)} \right|_{\mathbf{h}=0} = \langle \mathcal{T} \hat{O}_i(\tau) \hat{O}_j(\tau') \rangle - \langle \hat{O}_i \rangle \langle \hat{O}_j \rangle. \quad (1.40)$$

On the two-particle level, only the density’s response to variations in the one-particle energy, χ_d , and the magnetization’s response to variation in the electromagnetic field in the same direction, χ_m , are non-zero [**kappl susc**],

$$\chi_d(\tau) = \chi_{nn}(\tau) = -\left. \frac{\delta \langle \hat{n} \rangle}{\delta \mu(\tau)} \right|_{\mu=0} \quad \text{and} \quad (1.41a)$$

$$\chi_m(\tau) = \chi_{ii}(\tau) = \left. \frac{\delta \langle \hat{\sigma}_i \rangle}{\delta h_i(\tau)} \right|_{\mathbf{h}=0}, \quad (1.41b)$$

^[7]For example an external electromagnetic field.

where $i \in \{x, y, z\}$. The physical susceptibilities are included in the two-particle Green's function, as we will see shortly. In fact, the sum of terms corresponding to the two disconnected, horizontal Green's function lines and the vertex part is denoted as the general susceptibility and can be expressed as

$$\begin{aligned}\chi_{1234}^{qkk'} &= \beta \left(G_{1234}^{qkk'} - \delta_{q0} G_{12}^k G_{34}^{k'} \right) \\ &= -\beta \delta_{kk'} G_{14}^k G_{32}^{k-q} - \sum_{abcd} G_{1a}^k G_{b2}^{k-q} F_{abcd}^{qkk'} G_{3c}^{k'-q} G_{d4}^{k'} \\ &= \chi_{0;1234}^{qkk'} - \frac{1}{\beta^2} \sum_{abcd} \chi_{0;12ba}^{qkk} F_{abcd}^{qkk'} \chi_{0;dca3}^{qk'k'}\end{aligned}\quad (1.42)$$

where

$$\chi_{0;1234}^{qkk'} = -\beta \delta_{kk'} G_{14}^k G_{32}^{k-q} \quad (1.43)$$

is commonly denoted as the generalized bubble susceptibility. From this one can obtain physical susceptibilities by contracting the inner legs, i.e.,

$$\chi_{14}^q = \sum_{kk';23} \chi_{1234}^{qkk'}. \quad (1.44)$$

The diagrammatic content of the physical susceptibility is shown in Fig. 1.9 below. Similarly, the con-

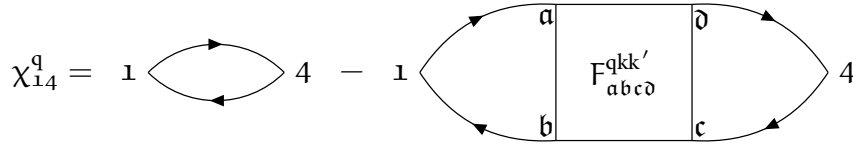


FIGURE 1.9 – The physical susceptibility is defined as the generalized susceptibility with contracted legs, see Eq. (1.44).

tracted bubble susceptibility can be written as

$$\chi_{0;14}^q = \sum_{kk';23} \chi_{0;1234}^{qkk'}. \quad (1.45)$$

Analogously to Eq. (1.25a) and Eq. (1.25d), one can write down density and magnetic spin combinations,

$$\chi_d^q = \chi_{\uparrow\uparrow}^q + \chi_{\uparrow\downarrow}^q = \chi_{\uparrow\downarrow}^q \quad \text{and} \quad (1.46a)$$

$$\chi_m^q = \chi_{\uparrow\uparrow}^q - \chi_{\uparrow\downarrow}^q. \quad (1.46b)$$

Note that expressions Eq. (1.46a) and Eq. (1.46b) are nothing more than the Fourier-transformed versions of Eq. (1.41a) and Eq. (1.41b), respectively.

1.5 Vertex asymptotics

A full treatment of frequency and momentum dependence of multi-orbital vertex functions severely restricts the speed and memory consumption of numerical calculations. A step towards reducing the computational cost of numerical implementations of equations involving vertex functions, such as the Bethe-Salpeter equations, see Sec. 1.6, or the Schwinger-Dyson equation, see Sec. 1.7, thus requires

an efficient treatment of the vertex for high Matsubara frequencies. We will see that the vertex - in the high-frequency regime - which originally depended on three independent frequency parameters can be treated as an object with only two frequency dimensions, thus drastically reducing the storage capacity of and ease of calculations including the vertex. But first, let us sketch the basic idea on how to tackle explicit asymptotic behaviour in vertex functions.

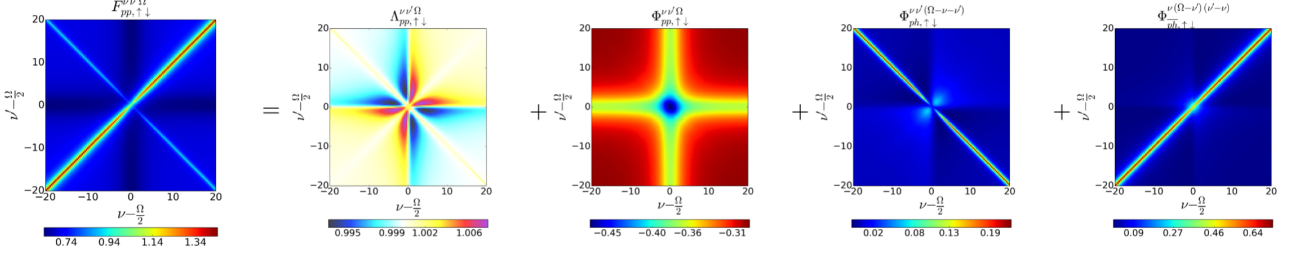


FIGURE 1.10 – Numerical SIAM results for all local vertices contained in the parquet equation Eq. (1.33) for vanishing transfer frequency $\Omega = 0$, taken from Ref. [high-freq asympt]. In our convention, Ω should be replaced by ω .

In Fig. 1.10, the frequency dependence of local vertex functions $F_{pp, \uparrow \downarrow}^{\omega \nu \nu'}$, $\Lambda_{pp, \uparrow \downarrow}^{\omega \nu \nu'}$ and $\Phi_{r, \uparrow \downarrow}^{\omega \nu \nu'}$ calculated for the Single-Impurity Anderson Model (SIAM) are shown for vanishing transfer frequency ω [high-freq asympt]. From this, one can see three very prominent and distinct features of the full vertex F : (i) a constant background that differs from the (local and constant) Hubbard interaction U ; (ii) two diagonal structures, the main ($\nu = \nu'$) and secondary ($\nu = -\nu'$) diagonal; and (iii) a “cross”-like structure along $\nu = \pm \frac{\pi}{\beta}$ and $\nu' = \pm \frac{\pi}{\beta}$. While only shown for the antiparallel spin combination $\uparrow \downarrow$ and vanishing transfer frequency $\omega = 0$, the features are analogous for the parallel spin combination $\uparrow \uparrow$ and for finite ω . These three attributes do *not* decay for high Matsubara frequencies ν and ν' and therefore indicate complex asymptotic behaviour. The individual asymptotic contributions of the fully irreducible vertex Λ and the reducible vertex in channel r to the full vertex F are written in detail in Ref. [high-freq asympt]. Summarized, Λ adds a constant background of size U , Φ_{ph} adds a secondary diagonal structure, $\Phi_{\overline{ph}}$ adds a diagonal structure and Φ_{pp} adds a constant background and a “cross”-like structure. Notice that the description in Ref. [high-freq asympt] only refers to the SIAM model and considers solely the one-band case with local quantities and a constant local interaction U . An extension to a multi-orbital formalism and momentum-dependent vertices and interaction U follows naturally and will be discussed shortly.

The simplest quantity to describe in terms of their asymptotics is the fully irreducible vertex $\Lambda_{1234}^{qkk'}$, for which

$$\Lambda_{1234; \sigma \sigma'}^{\text{asympt}; qkk'} \approx \mathcal{U}_{1234; \sigma \sigma'}^{qkk'}, \quad (1.47)$$

where $\mathcal{U}_{1234; \sigma \sigma'}^{qkk'}$ is the non-local Coulomb interaction, written in crossing-symmetric notation

$$\mathcal{U}_{1234; \sigma \sigma'}^{qkk'} = \frac{1}{\beta^2} \left[\underbrace{U_{1234} + V_{1234}^q}_{\mathcal{U}_{1234}^q} - \delta_{\sigma \sigma'} \left(\underbrace{U_{2314} + V_{2314}^{k'-k}}_{\tilde{\mathcal{U}}_{1234}^{k'-k}} \right) \right], \quad (1.48)$$

containing the purely local interaction U and the purely non-local interaction V . Eq. (1.48) is diagrammatically displayed in Fig. 1.11. Constructing d , m , s and t combinations of Eq. (1.48) is useful for future calculations,

$$\mathcal{U}_{d; 1234}^{qkk'} = \frac{1}{\beta^2} \left[2\mathcal{U}_{1234}^q - \tilde{\mathcal{U}}_{1234}^{k'-k} \right], \quad (1.49a)$$

$$\mathcal{U}_{1234;\sigma\sigma'}^{\mathbf{q}\mathbf{k}\mathbf{k}'} \equiv \sigma \frac{1}{2} \left(\mathcal{U}_{1234;\sigma\sigma'}^{\mathbf{q}\mathbf{k}\mathbf{k}'} \right) \frac{4}{3} \sigma' = \frac{2}{1} \frac{\mathcal{U}_{1234}^{\mathbf{q}}}{3} \frac{3}{4} - \delta_{\sigma\sigma'} \tilde{\mathcal{U}}_{1234}^{\mathbf{k}'-\mathbf{k}}$$

FIGURE 1.11 – Crossing-symmetric interaction, modulo a factor $\frac{1}{\beta^2}$, see Eq. (1.48).

$$\mathcal{U}_{\text{m};1234}^{\mathbf{q}\mathbf{k}\mathbf{k}'} = -\frac{1}{\beta^2} \tilde{\mathcal{U}}_{1234}^{\mathbf{k}'-\mathbf{k}}, \quad (1.49b)$$

$$\mathcal{U}_{\text{s};1234}^{\mathbf{q}\mathbf{k}\mathbf{k}'} = \frac{1}{\beta^2} \left[\mathcal{U}_{1234}^{\mathbf{k}+\mathbf{k}'-\mathbf{q}} + \tilde{\mathcal{U}}_{1234}^{\mathbf{k}'-\mathbf{k}} \right] \quad \text{and} \quad (1.49c)$$

$$\mathcal{U}_{\text{t};1234}^{\mathbf{q}\mathbf{k}\mathbf{k}'} = \frac{1}{\beta^2} \left[\mathcal{U}_{1234}^{\mathbf{k}+\mathbf{k}'-\mathbf{q}} - \tilde{\mathcal{U}}_{1234}^{\mathbf{k}'-\mathbf{k}} \right]. \quad (1.49d)$$

Next, we begin examining the diagrams contributing to Φ_{r} . A smart choice introduced in Ref. [**high-freq asympt**] is to classify these diagrams in each channel further into three categories:

- Class 1: These are diagrams which connect incoming and outgoing particles only by a single interaction vertex. These diagrams are bubble diagrams and hence only depend on a single bosonic frequency and momentum. The sum of all these diagrams will be encoded in the variable $\mathcal{K}_{\text{r};1234;\sigma\sigma'}^{(1);\mathbf{q}}$, see the first line in Fig. 1.12.
- Class 2: Diagrams corresponding to class 2 are identified by them having either the incoming *or* outgoing particles connected to the same interaction vertex. These diagrams depend on the bosonic transfer frequency and momentum and one fermionic frequency and momentum. The sum of all these diagrams will be encoded in the variables $\mathcal{K}_{\text{r};1234;\sigma\sigma'}^{(2);\mathbf{q}\mathbf{k}}$ and $\bar{\mathcal{K}}_{\text{r};1234;\sigma\sigma'}^{(2);\mathbf{q}\mathbf{k}}$, depending on whether the outgoing particles (\mathcal{K}) or the incoming particles ($\bar{\mathcal{K}}$) are connected to the interaction vertex, see the second line in Fig. 1.12. \mathcal{K} and $\bar{\mathcal{K}}$ are related to each other via time-reversal symmetry, where in the case of a system with additional SU(2)-symmetry corresponds to [**rohringer thesis**] $\mathcal{K}_{\text{r};1234;\sigma\sigma'}^{(2);\mathbf{q}\mathbf{k}} = \bar{\mathcal{K}}_{\text{r};1234;\sigma\sigma'}^{(2);\mathbf{q}\mathbf{k}}$.
- Class 3: These are diagrams where each external Green's function is connected to a different interaction vertex. These diagrams are parametrized by three independent frequency and momentum arguments and are encoded in the “rest” function $\mathcal{R}_{\text{r};1234;\sigma\sigma'}^{\mathbf{q}\mathbf{k}\mathbf{k}'}$.

In the following, we will refer to $\mathcal{K}^{(1)}$, $\mathcal{K}^{(2)}$ and $\bar{\mathcal{K}}^{(2)}$ as kernel functions. One now can - with the help of these classifications - write the reducible Φ_{r} -vertices as a decomposition of the different kernel functions and the “rest”-function

$$\Phi_{\text{r};1234;\sigma\sigma'}^{\mathbf{q}\mathbf{k}\mathbf{k}'} = \mathcal{K}_{\text{r};1234;\sigma\sigma'}^{(1);\mathbf{q}} + \mathcal{K}_{\text{r};1234;\sigma\sigma'}^{(2);\mathbf{q}\mathbf{k}} + \mathcal{K}_{\text{r};1234;\sigma\sigma'}^{(2);\mathbf{q}\mathbf{k}'} + \mathcal{R}_{\text{r};1234;\sigma\sigma'}^{\mathbf{q}\mathbf{k}\mathbf{k}'}. \quad (1.50)$$

This composition is *per se* exact. However, to take advantage of this formalism for numerical calculations, one discards the “rest”-function due to its additional frequency dependence entering the inner propagators, resulting in a quicker drop-off in all frequency directions. Thus, the approximation

$$\Phi_{\text{r};1234;\sigma\sigma'}^{\text{asympt};\mathbf{q}\mathbf{k}\mathbf{k}'} \approx \mathcal{K}_{\text{r};1234;\sigma\sigma'}^{(1);\mathbf{q}} + \mathcal{K}_{\text{r};1234;\sigma\sigma'}^{(2);\mathbf{q}\mathbf{k}} + \mathcal{K}_{\text{r};1234;\sigma\sigma'}^{(2);\mathbf{q}\mathbf{k}'} \quad (1.51)$$

serves as a valid expression for the high-frequency regime of Φ_{r} and becomes exact for $\nu, \nu' \rightarrow \infty$ [**high-freq asympt**]. As we can see above, the quantities on the right hand side of Eq. (1.51) only depend on two Matsubara frequencies instead of three, reducing the numerical complexity and memory

usage for Φ_r significantly. Using these explicit asymptotics results in a tremendous improvement of numerical results over a simple truncation in Φ_r for high frequencies [**high-freq asympt**]. The kernel functions needed to calculate the reducible diagrams can be obtained by [**towards ab initio dga, josef DA, pudleiner paper**]

$$\mathcal{K}_{\text{ph};1234;\sigma\sigma'}^{(1);q} = \sum_{\substack{abcd;k_1 k_2 \\ \sigma_1 \sigma_2}} \mathcal{U}_{12ab;\sigma\sigma_1}^{\mathbf{q}k_1} \chi_{ba\bar{d}c;\sigma_1 \sigma_2}^{\mathbf{q}k_1 k_2} \mathcal{U}_{\bar{c}d34;\sigma_2 \sigma'}^{\mathbf{q}(-k_2)}, \quad (1.52)$$

$$\mathcal{K}_{\text{pp};1234;\sigma\sigma'}^{(1);q} = \frac{1}{4} \sum_{\substack{abcd;k_1 k_2 \\ \sigma_1 \sigma_2 \sigma_3 \sigma_4}} \mathcal{U}_{1b3a}^{\mathbf{q}k_1} \chi_{ac\bar{b}d}^{\mathbf{q}k_1 k_2} \mathcal{U}_{\bar{d}2c4}^{\mathbf{q}(-k_2)} \mathcal{U}_{\sigma_4 \sigma \sigma_3 \sigma'}^{\mathbf{q}(-k_2)}, \quad (1.53)$$

$$\begin{aligned} \mathcal{K}_{\text{ph};1234;\sigma\sigma'}^{(2);qk} &= \sum_{\substack{ab;k_1 \\ \sigma_1}} F_{12ab;\sigma\sigma_1}^{\mathbf{q}kk_1} \chi_{0;\bar{b}a\bar{a}b}^{\mathbf{q}k_1 k_1} \mathcal{U}_{ba34;\sigma_1 \sigma'}^{\mathbf{q}(-k_1)} - \mathcal{K}_{\text{ph};1234;\sigma\sigma'}^{(1);q} \\ &= - \sum_{\substack{ab;k_1 \\ \sigma_1}} \frac{\chi_{\bar{c}dab;\sigma\sigma_1}^{\mathbf{q}kk_1}}{G_{c1}^k G_{2d}^{k-q}} \mathcal{U}_{ba34;\sigma_1 \sigma'}^{\mathbf{q}(-k_1)} - \mathcal{K}_{\text{ph};1234;\sigma\sigma'}^{(1);q} \end{aligned} \quad (1.54)$$

$$\begin{aligned} \mathcal{K}_{\text{pp};1234;\sigma\sigma'}^{(2);qk} &= \frac{1}{2} \sum_{\substack{ab;k_1 \\ \sigma_1 \sigma_2 \sigma_3 \sigma_4}} F_{\text{pp};1a3b}^{\mathbf{q}kk_1} \chi_{0;\bar{b}a\bar{a}b}^{\mathbf{q}k_1 k_1} \mathcal{U}_{b2a4}^{\mathbf{q}(-k_1)} \mathcal{U}_{\sigma_2 \sigma \sigma_1 \sigma'}^{\mathbf{q}(-k_1)} - \mathcal{K}_{\text{pp};1234;\sigma\sigma'}^{(1);q} \\ &= - \frac{1}{2} \sum_{\substack{abcd;k_1 \\ \sigma_1 \sigma_2 \sigma_3 \sigma_4}} \frac{\chi_{\text{pp};ca\bar{d}b}^{\mathbf{q}kk_1}}{G_{1c}^k G_{3d}^{k-q}} \mathcal{U}_{b2a4}^{\mathbf{q}(-k_1)} \mathcal{U}_{\sigma_2 \sigma \sigma_1 \sigma'}^{\mathbf{q}(-k_1)} - \mathcal{K}_{\text{pp};1234;\sigma\sigma'}^{(1);q} \end{aligned} \quad (1.55)$$

where the subtraction of $\mathcal{K}^{(1)}$ in the kernel-2 function is to account for double-counting of diagrams and $\mathcal{U}_{1234;\sigma\sigma'}^{\mathbf{q}k'}$ is obtained from Eq. (1.48) by setting $\mathbf{k} = \mathbf{0}$. Both kernel functions are displayed diagrammatically for the ph-channel in Fig. 1.12. The density and magnetic contributions to the kernel

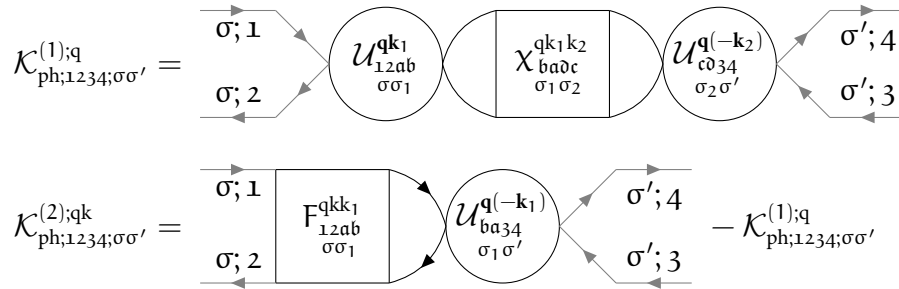


FIGURE 1.12 – Diagrammatic version of the kernel-1 and kernel-2 functions of Eq. (1.52) and Eq. (1.54).

functions read

$$\mathcal{K}_{d;1234}^{(1);q} = \sum_{\substack{abcd \\ k_1 k_2}} \mathcal{U}_{d;12ab}^{\mathbf{q}k_1} \chi_{d;\bar{b}a\bar{d}c}^{\mathbf{q}k_1 k_2} \mathcal{U}_{d;\bar{c}d34}^{\mathbf{q}(-k_2)}, \quad (1.56a)$$

$$\mathcal{K}_{m;1234}^{(1);q} = \sum_{\substack{abcd \\ k_1 k_2}} \mathcal{U}_{m;12ab}^{\mathbf{q}k_1} \chi_{m;\bar{b}a\bar{d}c}^{\mathbf{q}k_1 k_2} \mathcal{U}_{m;\bar{c}d34}^{\mathbf{q}(-k_2)}, \quad (1.56b)$$

$$\begin{aligned}
\mathcal{K}_{d;1234}^{(2);qk} &= \sum_{ab;k_1} F_{d;12ab}^{qkk_1} \chi_{0;baab}^{qk_1 k_1} \mathcal{U}_{d;ba34}^{q(-k_1)} - \mathcal{K}_{d;1234}^{(1);q} \\
&= - \sum_{abc\bar{d};k_1} \frac{\chi_{d;c\bar{d}ab}^{qkk_1}}{G_{c1}^k G_{2\bar{d}}^{k-q}} \mathcal{U}_{d;ba34}^{q(-k_1)} - \mathcal{K}_{d;1234}^{(1);q} \quad \text{and}
\end{aligned} \tag{1.56c}$$

$$\begin{aligned}
\mathcal{K}_{m;1234}^{(2);qk} &= \sum_{ab;k_1} F_{m;12ab}^{qkk_1} \chi_{0;baab}^{qk_1 k_1} \mathcal{U}_{m;ba34}^{q(-k_1)} - \mathcal{K}_{m;1234}^{(1);q} \\
&= - \sum_{abc\bar{d};k_1} \frac{\chi_{m;c\bar{d}ab}^{qkk_1}}{G_{c1}^k G_{2\bar{d}}^{k-q}} \mathcal{U}_{m;ba34}^{q(-k_1)} - \mathcal{K}_{m;1234}^{(1);q}.
\end{aligned} \tag{1.56d}$$

The s/t combinations can be constructed analogously for the pp-channel (written in pp frequency notation):

$$\mathcal{K}_{s;1234}^{(1);q} = \frac{1}{4} \sum_{\substack{abcd \\ k_1 k_2}} \mathcal{U}_{s;1b3a}^{qk_1} \chi_{s;acbd}^{qk_1 k_2} \mathcal{U}_{s;2c4}^{q(-k_2)}, \tag{1.57a}$$

$$\mathcal{K}_{t;1234}^{(1);q} = \frac{1}{4} \sum_{\substack{abcd \\ k_1 k_2}} \mathcal{U}_{t;1b3a}^{qk_1} \chi_{t;acbd}^{qk_1 k_2} \mathcal{U}_{t;2c4}^{q(-k_2)}, \tag{1.57b}$$

$$\begin{aligned}
\mathcal{K}_{s;1234}^{(2);qk} &= \frac{1}{2} \sum_{ab;k_1} F_{s;1a3b}^{qkk_1} \chi_{0;baab}^{qk_1 k_1} \mathcal{U}_{s;b2a4}^{q(-k_1)} - \mathcal{K}_{s;1234}^{(1);q} \\
&= -\frac{1}{2} \sum_{abc\bar{d};k_1} \frac{\chi_{s;c\bar{d}ab}^{qkk_1}}{G_{1c}^k G_{3\bar{d}}^{k-q}} \mathcal{U}_{s;b2a4}^{q(-k_1)} - \mathcal{K}_{s;1234}^{(1);q} \quad \text{and}
\end{aligned} \tag{1.57c}$$

$$\begin{aligned}
\mathcal{K}_{t;1234}^{(2);qk} &= \frac{1}{2} \sum_{ab;k_1} F_{t;1a3b}^{qkk_1} \chi_{0;baab}^{qk_1 k_1} \mathcal{U}_{t;b2a4}^{q(-k_1)} - \mathcal{K}_{t;1234}^{(1);q} \\
&= -\frac{1}{2} \sum_{abc\bar{d};k_1} \frac{\chi_{t;c\bar{d}ab}^{qkk_1}}{G_{1c}^k G_{3\bar{d}}^{k-q}} \mathcal{U}_{t;b2a4}^{q(-k_1)} - \mathcal{K}_{t;1234}^{(1);q}.
\end{aligned} \tag{1.57d}$$

Finally, the asymptotic part of the full vertex $(F_{r;1234;\sigma\sigma'}^{\text{asympt};qkk'})$ can now be assembled using the asymptotic contributions of $\Lambda_{1234;\sigma\sigma'}^{\text{asympt};qkk'}$ and $\Phi_{r;1234;\sigma\sigma'}^{\text{asympt};qkk'}$ through the parquet decomposition of Eq. (1.33). This results in

$$F_{1234;\sigma\sigma'}^{\text{asympt};qkk'} - \mathcal{U}_{1234;\sigma\sigma'}^{qkk'} = \Phi_{ph;1234;\sigma\sigma'}^{\text{asympt};qkk'} + \Phi_{\bar{ph};1234;\sigma\sigma'}^{\text{asympt};qkk'} + \Phi_{pp;1234;\sigma\sigma'}^{\text{asympt};qkk'}, \tag{1.58}$$

or explicitly with kernel-1 and kernel-2 functions,

$$\begin{aligned}
F_{1234;\sigma\sigma'}^{\text{asympt};qkk'} - \mathcal{U}_{1234;\sigma\sigma'}^{qkk'} &= \mathcal{K}_{ph;1234;\sigma\sigma'}^{(1);q} + \mathcal{K}_{ph;1234;\sigma\sigma'}^{(2);qk} + \mathcal{K}_{ph;1234;\sigma\sigma'}^{(2);qk'} \\
&\quad + \mathcal{K}_{\bar{ph};1234;\sigma\sigma'}^{(1);q} + \mathcal{K}_{\bar{ph};1234;\sigma\sigma'}^{(2);qk} + \mathcal{K}_{\bar{ph};1234;\sigma\sigma'}^{(2);qk'} \\
&\quad + \mathcal{K}_{pp;1234;\sigma\sigma'}^{(1);q} + \mathcal{K}_{pp;1234;\sigma\sigma'}^{(2);qk} + \mathcal{K}_{pp;1234;\sigma\sigma'}^{(2);qk'}.
\end{aligned} \tag{1.59}$$

The asymptotic behavior of the irreducible vertex in channel r follows from Eq. (1.34),

$$\Gamma_{r;1234;\sigma\sigma'}^{\text{asympt};qkk'} = F_{1234;\sigma\sigma'}^{\text{asympt};qkk'} - \Phi_{r;1234;\sigma\sigma'}^{\text{asympt};qkk'} \tag{1.60}$$

and reads for the ph-channel explicitly

$$\begin{aligned}
\Gamma_{ph;1234;\sigma\sigma'}^{\text{asympt};qkk'} &= \mathcal{U}_{1234;\sigma\sigma'}^{qkk'} + \Phi_{ph;1234;\sigma\sigma'}^{\text{asympt};qkk'} + \Phi_{pp;1234;\sigma\sigma'}^{\text{asympt};qkk'} \\
&= \mathcal{U}_{1234;\sigma\sigma'}^{qkk'} - \Phi_{ph;3214;\sigma'\bar{\sigma}}^{\text{asympt};(k'-k)(k'-q)k'} + \Phi_{pp;1234;\sigma\sigma'}^{\text{asympt};(k+k'-q)kk'},
\end{aligned} \tag{1.61}$$

where we used Eq. (1.36) to transform the $\overline{\text{ph}}$ -channel reducible vertex to a ph-channel reducible one. From this follows the irreducible vertex in the density and magnetic channel (in ph frequency notation) [**efficient BSE**]

$$\Gamma_{d;1234}^{\text{asympt};qkk'} = \mathcal{U}_{d;1234}^{qkk'} - \frac{1}{2} \Phi_{d;3214}^{\text{asympt};(k'-k)(k'-q)k'} - \frac{3}{2} \Phi_{m;3214}^{\text{asympt};(k'-k)(k'-q)k'} + \frac{1}{2} \Phi_{s;1234}^{\text{asympt};(k+k'-q)kk'} + \frac{3}{2} \Phi_{t;1234}^{\text{asympt};(k+k'-q)kk'}, \quad (1.62a)$$

$$\Gamma_{m;1234}^{\text{asympt};qkk'} = \mathcal{U}_{m;1234}^{qkk'} - \frac{1}{2} \Phi_{d;3214}^{\text{asympt};(k'-k)(k'-q)k'} + \frac{1}{2} \Phi_{m;3214}^{\text{asympt};(k'-k)(k'-q)k'} - \frac{1}{2} \Phi_{s;1234}^{\text{asympt};(k+k'-q)kk'} + \frac{1}{2} \Phi_{t;1234}^{\text{asympt};(k+k'-q)kk'}, \quad (1.62b)$$

where the $\Phi_{r;1234}^{\text{asympt};qkk'}$ are given by the kernel functions of Eq. (1.56) and Eq. (1.57). The irreducible vertices in channels $\overline{\text{ph}}$ and $\overline{\text{pp}}$ in m/d and s/t combinations can be constructed analogously.

1.6 Bethe-Salpeter equation

In the section above we have specified $\Gamma_{r;1234}^{qkk'}$ as the fully irreducible vertex in channel r and $\Phi_{r;1234}^{qkk'}$ as the reducible diagrams in channel r. We can now construct the full set of $\Phi_{r;1234}^{qkk'}$ from the irreducible vertex by chaining them together with pairs of Green's functions connecting two irreducible vertices. This results in so-called ladders,

$$\begin{aligned} \Phi_{r;1234}^{qkk'} &= \sum_{k_1;abcd} \Gamma_{r;12ab}^{qkk_1} G_{bc}^{k_1} G_{da}^{k_1-q} \Gamma_{r;c\bar{d}34}^{qk_1k'} \\ &+ \sum_{k_1k_2;abcd} \Gamma_{r;12ab}^{qkk_1} G_{bc}^{k_1} G_{da}^{k_1-q} \Gamma_{r;c\bar{d}ef}^{qk_1k_2} G_{fg}^{k_2} G_{he}^{k_2-q} \Gamma_{r;gh34}^{qk_2k'} + \dots \end{aligned} \quad (1.63a)$$

$$\begin{aligned} &= -\frac{1}{\beta} \sum_{k_1;abcd} \Gamma_{r;12ab}^{qkk_1} \chi_{0;b\bar{a}d\bar{c}}^{qk_1k_1} \Gamma_{r;c\bar{d}34}^{qk_1k'} \\ &+ \frac{1}{\beta^2} \sum_{k_1k_2;abcd} \Gamma_{r;12ab}^{qkk_1} \chi_{0;b\bar{a}d\bar{c}}^{qk_1k_1} \Gamma_{r;c\bar{d}ef}^{qk_1k_2} \chi_{0;f\bar{e}h\bar{g}}^{qk_2k_2} \Gamma_{r;gh34}^{qk_2k'} + \dots \end{aligned} \quad (1.63b)$$

By combining Eq. (1.34) and Eq. (1.63), one can obtain the Bethe-Salpeter equation (BSE) in all three channels [**a relativistic equation for bound-state, nambu paper, rohringer thesis maybe**],

$$F_{1234}^{qkk'} = \Gamma_{ph;1234}^{qkk'} - \frac{1}{\beta} \sum_{k_1k_2;abcd} \Gamma_{ph;12ba}^{qkk_1} \chi_{0;a\bar{b}c\bar{d}}^{qk_1k_2} F_{ph;\bar{d}c34}^{qk_2k'} \quad (1.64a)$$

$$= \Gamma_{\overline{\text{ph}};1234}^{qkk'} + \frac{1}{\beta} \sum_{k_1k_2;abcd} \Gamma_{\overline{\text{ph}};12ba}^{qkk_1} \chi_{0;a\bar{b}c\bar{d}}^{qk_1k_2} F_{\overline{\text{ph}};\bar{d}c34}^{qk_2k'} \quad (1.64b)$$

$$= \Gamma_{pp;1234}^{qkk'} - \frac{1}{2\beta} \sum_{k_1k_2;abcd} \Gamma_{pp;12ba}^{qkk_1} \chi_{0;a\bar{b}c\bar{d}}^{qk_1k_2} F_{pp;\bar{d}c34}^{qk_2k'}, \quad (1.64c)$$

where we have expressed the full vertex $F_{1234}^{qkk'}$ in terms of the irreducible vertex $\Gamma_{r;1234}^{qkk'}$ and the generalized (bubble) susceptibility as a Dyson-like equation. Note that for Eq. (1.64) we used the same channel reducibility and frequency notation for each separate line. This results in a key property of

the BSE: the equation becomes diagonal in the bosonic transfer momentum and frequency q . This can be taken advantage of in numerical computations as it makes it especially easy to parallelize over q as it is independent of all other quantum numbers. If we had not chosen the channel reducibility equal to the frequency notation, then the new q' would depend on the fermionic frequencies (the precise dependency is channel-specific, but in general $q' = f(q, k, k')$) and the transformed BSE would not be diagonal in q' .

Eq. (1.64) can be rewritten in terms of susceptibilities with the help of Eq. (1.42),

$$\chi_{1234}^{qkk'} = \chi_{0;1234}^{qkk'} - \frac{1}{\beta^2} \sum_{k_1 k_2; abc d} \chi_{0;12ba}^{qkk_1} \Gamma_{ph;abc d}^{qk_1 k_2} \chi_{ph;dc34}^{qk_2 k'} \quad (1.65a)$$

$$= \chi_{0;1234}^{qkk'} + \frac{1}{\beta^2} \sum_{k_1 k_2; abc d} \chi_{0;12ba}^{qkk_1} \Gamma_{ph;abc d}^{qk_1 k_2} \chi_{ph;dc34}^{qk_2 k'} \quad (1.65b)$$

$$= \chi_{0;1234}^{qkk'} - \frac{1}{2\beta^2} \sum_{k_1 k_2; abc d} \chi_{0;1c3a}^{qkk_1} \Gamma_{pp;abc d}^{qk_1 k_2} (\chi_{pp;d2b4}^{qk_2 k'} + \chi_{0;d2b4}^{qk_2 k'}). \quad (1.65c)$$

This is the most general form of the Bethe-Salpeter equations, where energy and momentum is conserved. If the system under consideration is additionally SU(2)-symmetric, then we can formulate the BSE in terms of density and magnetic spin components,

$$F_{d/m;ph;1234}^{qkk'} = \Gamma_{d/m;ph;1234}^{qkk'} - \frac{1}{\beta} \sum_{k_1 k_2; abc d} \Gamma_{d/m;ph;12ba}^{qkk_1} \chi_{0;abc d}^{qk_1 k_2} F_{d/m;ph;dc34}^{qk_2 k'} \quad \text{and} \quad (1.66a)$$

$$F_{d/m;ph;1234}^{qkk'} = \Gamma_{d/m;ph;1234}^{qkk'} - \frac{1}{\beta} \sum_{k_1 k_2; abc d} \Gamma_{d/m;ph;12ba}^{qkk_1} \chi_{0;abc d}^{qk_1 k_2} F_{d/m;ph;dc34}^{qk_2 k'}. \quad (1.66b)$$

Likewise, the BSE decouples for other spin-symmetric combinations in for the pp-channel. These are the (s)inglet and (t)riplet channel, where

$$F_{s;pp;1234}^{qkk'} = \Gamma_{s;pp;1234}^{qkk'} + \frac{1}{2\beta} \sum_{k_1 k_2; abc d} \Gamma_{s;pp;12ba}^{qkk_1} \chi_{0;abc d}^{qk_1 k_2} F_{s;pp;dc34}^{qk_2 k'} \quad \text{and} \quad (1.67)$$

$$F_{t;pp;1234}^{qkk'} = \Gamma_{t;pp;1234}^{qkk'} - \frac{1}{2\beta} \sum_{k_1 k_2; abc d} \Gamma_{t;pp;12ba}^{qkk_1} \chi_{0;abc d}^{qk_1 k_2} F_{t;pp;dc34}^{qk_2 k'}. \quad (1.68)$$

For a visual representation of the Bethe-Salpeter equation (1.64), see Fig. 1.13. The BSE of Eq. (1.64) needs to be inverted in order to be able to yield the full vertex $F_{1234}^{qkk'}$. This can be done in a smart way by viewing the multiplications of the vertex functions in the BSE as matrix multiplications written down in grouped indices. This means that for each transfer momentum q , we can generate a matrix from a vertex by grouping the left (right) two orbital indices and fermionic frequencies into a new grouped index $n = \{n_1, n_2, k\}$ ($m = \{n_3, n_4, k'\}$), such that [**ab initio dyn**]

$$\mathbf{F}_{nm}^q = F_{1234}^{qkk'}. \quad (1.69)$$

This allows for a straightforward numerical implementation of vertex products and inversions with respect to these grouped indices. Hence, this yields for the full vertex $\mathbf{F}_{d/m;nm}^q$ obtained from the BSE,

$$\mathbf{F}_{d/m;nm}^q = \left(\mathbb{1}_{nm} + \frac{1}{\beta} \mathbf{F}_{d/m;nl}^q \chi_{0;lm}^q \right)^{-1}. \quad (1.70)$$

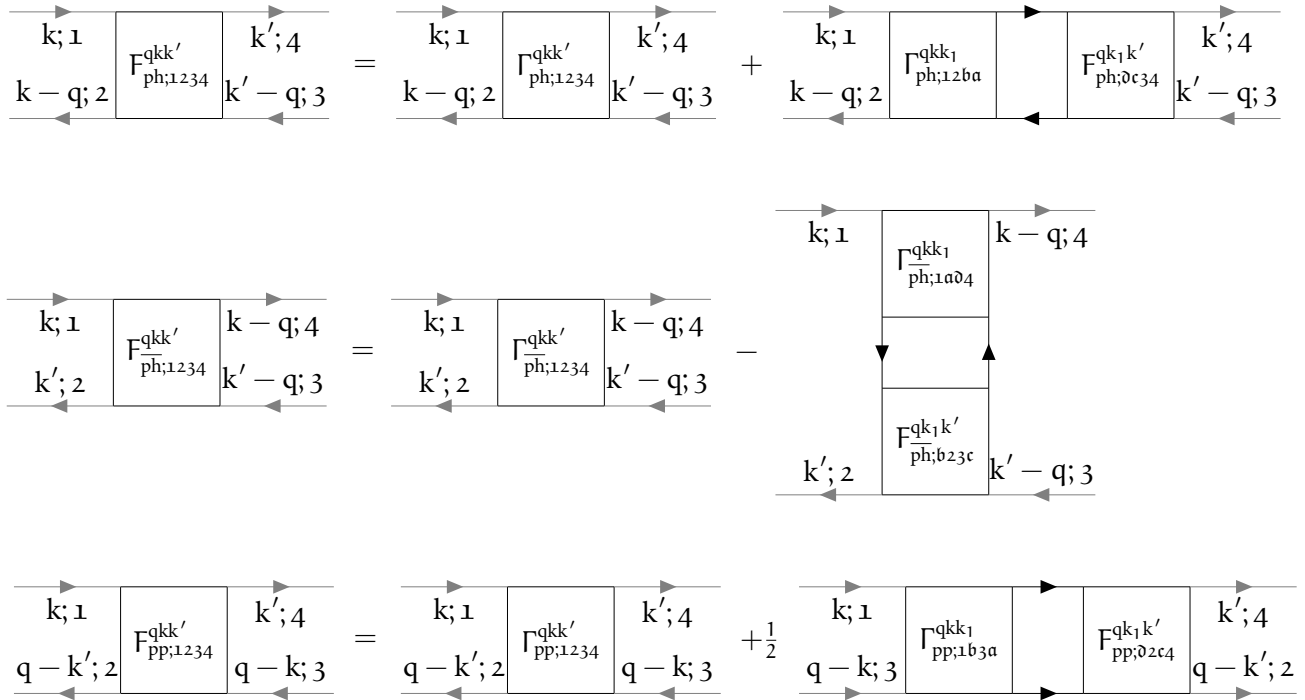


FIGURE 1.13 – Diagrammatic version of the BSE in all three channels for arbitrary spin components, see Eq. (1.64). The lower legs are exchanged in pp-notation, hence their direction is reversed.

1.6.1 High-frequency Bethe-Salpeter equation with vertex asymptotics

Sometimes it is convenient to separate low- and high-frequency components of a quantity to simplify calculations. Some DMFT solvers [**parragh**] employ such a frequency separation to calculate the self-energy: a high-frequency asymptotic expansion derived from the spectral function's lowest moments is incorporated in the numerical solution of the Dyson equation at low frequencies. Inspired by this idea, we can proceed similarly for the irreducible vertex Γ , working with the framework of the Bethe-Salpeter equation instead of the Dyson equation. By explicitly using the $SU(2)$ -symmetric combinations d, m — in which the BSE for the ph-channel becomes diagonal^[8] — we aim to reduce the computational effort by using a high-frequency expansion of the vertex functions. Following [**kunes asympt**, **hummel DA**, **efficient BSE**], the vertex in the low-frequency regime can be obtained by the regular BSE, where an additional high-frequency correction term is added. In the spirit of the end of last section, the BSE of Eq. (1.65) can be written as a matrix equation (in grouped indices nm) for channels d, m in the following fashion

$$\chi^q = \chi_0^q - \frac{1}{\beta^2} \chi_0^q \Gamma^q \chi^q. \quad (1.71)$$

Similar to Refs. [**kunes**, **hummel DA**, **efficient BSE**], we will now split the matrices F , Γ and χ in segments of low and high frequencies. We will denote this by an additional superscript (L/H, L/H), where (L, L) denotes the segment, where ν and ν' are in the low frequency region and, e.g., (L, H) denotes the segment, where ν is in the low- and ν' in the high-frequency region. We will therefore construct a set of low frequencies \mathcal{I}_L and a set of high frequencies \mathcal{I}_H . This means, that for Γ^{LH} , $\nu \in \mathcal{I}_L$ and $\nu' \in \mathcal{I}_H$. In the LH, HL and HH blocks, where atleast one frequency is considered large, we will employ explicit asymptotics for the vertex functions, as already discussed in Sec. 1.5. The goal

^[8]The same can be done for the s, t combinations in the pp-channel, however only the ph-channel will be shown.

is to calculate the vertex function with the BSE for the low-frequency region where we will expect a correction term arising from the low-frequency cutoff which employs the use of high-frequency blocks of the BSE components. The size of \mathcal{I}_L has to be atleast the number of bosonic Matsubara frequencies ω [**efficient BSE**] and might differ if non-local correlations are included [**kinza two-particle corr**]. Regarding \mathcal{I}_H , there is no minimum size and the maximum size of the high-frequency region is only bounded by the availability of computational resources and memory.

Using this idea, we will solve Eq. (1.71) for Γ as

$$\begin{pmatrix} \Gamma^{LL} & \Gamma^{LH} \\ \Gamma^{HL} & \Gamma^{HH} \end{pmatrix} = \beta^2 \left[\begin{pmatrix} \chi^{LL} & \chi^{LH} \\ \chi^{HL} & \chi^{HH} \end{pmatrix}^{-1} - \begin{pmatrix} \chi_0^{LL} & 0 \\ 0 & \chi_0^{HH} \end{pmatrix}^{-1} \right] \quad (1.72)$$

where we omitted frequency labels for brevity. Multiplying on the left by χ and solving this matrix-like equation for Γ^{LL} , we find

$$\Gamma^{LL} = \beta^2 \left[(\chi^{LL})^{-1} - (\chi_0^{LL})^{-1} \right] - (\chi^{LL})^{-1} \chi^{LH} \Gamma^{HL}, \quad (1.73)$$

with

$$\chi^{LH} = -\chi^{LL} \Gamma^{LH} \left[\Gamma^{HH} + \beta^2 (\chi_0^{HH})^{-1} \right]^{-1}. \quad (1.74)$$

Combining these two equations yields for Γ^{LL}

$$\Gamma^{LL} = \beta^2 \left[(\chi^{LL})^{-1} - (\chi_0^{LL})^{-1} \right] + \Gamma^{LH} \left[\Gamma^{HH} + \beta^2 (\chi_0^{HH})^{-1} \right]^{-1} \Gamma^{HL}. \quad (1.75)$$

The last term in the sum of Eq. (1.75) can be thought of as a correction to the inversion of the BSE in the low-frequency subspace, which otherwise reads

$$\Gamma^{LL} = \beta^2 \left[(\chi^{LL})^{-1} - (\chi_0^{LL})^{-1} \right]. \quad (1.76)$$

The correction term can be obtained at a significantly lower cost compared to the full vertex — since for the high-frequency regimes of Γ we use kernel-1 and kernel-2 functions, which depend on either one or two momentum and frequency dimension less (see Sec. 1.5) — and is therefore easily available for much larger frequency ranges. Other sets of equations for $\Gamma^{LL[9]}$ can be acquired easily by manipulating the original BSE (1.71). These methods would require the calculation (or knowledge) of the Fermi-Bose vertex and the generalized susceptibility (or the full vertex) for a large frequency range^[10], which is more storage-heavy than the use of kernel-1 and kernel-2 functions. Thus, the approach outlined in this thesis is more efficient and is going to be the most practical one to use for multi-orbital calculations. Some remarks for the calculation of the irreducible vertex Γ^{LL} in the low-frequency region $\mathcal{I}_L = [N_{\min}, N_{\max}]$: Ref. [**efficient bse**] suggests to consider frequency ranges for ν, ν' where the main structures of χ are centered, see also Ref. [**local corr at the two-particle level**]. This means, that for the ph-channel we have $N_{\max} + 1 = -N_{\min} - 2m$, where m denotes the index of the bosonic Matsubara frequency $\omega_m = \frac{2m\pi}{\beta}$. An illustration of the “core” and “asymptotic” frequency region is depicted in Fig. 1.14 below. The correction terms are taken in the (much) larger frequency range $\mathcal{I}_H = [M_{\min}, M_{\max}]$, which is chosen to be of appropriate size such that the equations converge with respect to the size of \mathcal{I}_H .

^[9]One can already use Eq. (1.73) instead of Eq. (1.75), cf. “Method 2” in Ref. [**efficient bse**].

^[10]Retrieving the vertex functions in a high-frequency regime is *per se* not difficult; they can be obtained for arbitrary frequency ranges from the impurity solver of choice. However, the computing time increases drastically the larger the frequency box and thus this method is not preferred over the one mentioned in this thesis.

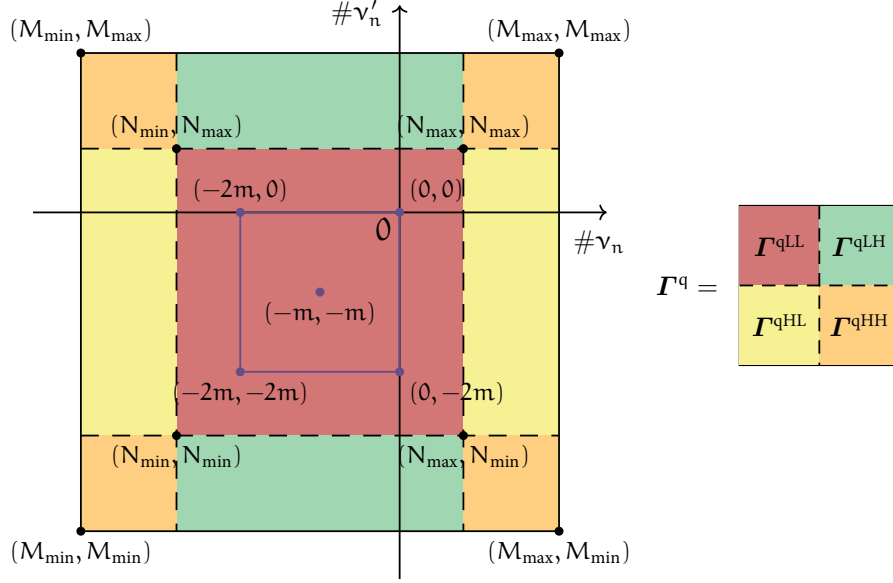


FIGURE 1.14 – Representation of the “block” construction used in Eq. (1.72). To keep the frequencies centered as described in [rohringer two particle level], we choose $N_{\min} = -\frac{N}{2} - m$, $N_{\max} = \frac{N}{2} - m - 1$, $M_{\min} = -\frac{M}{2} - m$ and $M_{\max} = \frac{M}{2} - m - 1$, where N is the size of the “core” and M the size of the “asymptotic” frequency region, respectively. This graphic has been taken from Ref. [efficient BSE] including some adaptations to fit the style of this thesis.

1.7 Schwinger-Dyson equation

To fill the missing gap in our (almost) complete theory of correlated electrons on a lattice, we have to consider the calculation of the self-energy which enters the many-body Green’s function through Eq. (1.18). This is done by the Schwinger-Dyson equation, which is derived as an equation of motion for the self-energy [rohringer thesis] and connects the self-energy to the full vertex via^[11] [anna galler thesis, ab initio dga]

$$\begin{aligned} \Sigma_{12}^k &= \Sigma_{\text{HF};12}^k + \Sigma_{12}^{\text{conn};k} \\ &= \underbrace{2 \sum_{ab;k'} \mathcal{U}_{12ab}^{q=0} n_{ba}^{k'}}_{\Sigma_{\text{HF};12}^k} - \underbrace{\sum_{ab,q} \mathcal{U}_{1ba2}^q n_{ba}^{k-q} - \frac{1}{\beta} \sum_{\substack{abcdef \\ qk'}} \mathcal{U}_{a1bc}^q \chi_{0;cbed}^{qk'k'} F_{de2f}^{qk'k} G_{af}^{k-q}}_{\Sigma_{12}^{\text{conn};k}}, \end{aligned} \quad (1.77)$$

where the first two sums in Eq. (1.77) are coined Hartree- and Fock-terms, respectively, and the third term is the vertex part and only contains connected diagrams. A visual representation of the Schwinger-Dyson equation can be seen in Fig. 1.15. The ph and $\overline{\text{ph}}$ contributions of the connected part yield separately (in ph notation)^[12] [ab initio dga]

$$\Sigma_{\text{ph};12}^{\text{conn};k} = -\frac{1}{\beta} \sum_{\substack{abcdef \\ qk'}} \mathcal{U}_{a1bc}^q \chi_{0;cbed}^{qk'k'} F_{d;de2f}^{qk'k} G_{af}^{k-q} \quad \text{and} \quad (1.78a)$$

^[11]In its most general form, the self-energy Σ also depends on the particle spin σ . In the SU(2)-symmetric case however we can omit the spin label, since $\Sigma_{\uparrow} = \Sigma_{\downarrow} = \Sigma$.

^[12]With the help of Eq. (1.37)

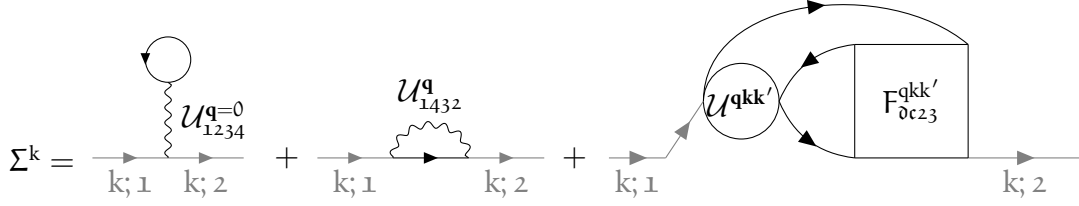


FIGURE 1.15 – Representation of the Schwinger-Dyson equation (1.77).

$$\Sigma_{\text{ph};12}^{\text{conn};\text{ph};k} = -\frac{1}{2\beta} \sum_{\substack{abcdef \\ qk'}} \tilde{U}_{a1bc}^{k'-k} \chi_{0;cbcd}^{qk'k'} \left[F_{d;2e\partial f}^{(k'-k)(k'-q)k'} + 3F_{m;2e\partial f}^{(k'-k)(k'-q)k'} \right] G_{af}^{k-q}. \quad (1.78b)$$

The self-energy Σ_{12}^k does not have to fulfill any crossing-symmetry relation, hence we do not use $\mathcal{U}_{1234;\sigma\sigma'}^{qkk'}$ from Eq. (1.48) here but rather the two terms with \mathcal{U} and $\tilde{\mathcal{U}}$ separately. The total self-energy is now the sum of the Hartree-Fock contribution and the $\text{ph}/\overline{\text{ph}}$ terms. We want to note that the Schwinger-Dyson equation can be rewritten in terms of three-leg vertices (also commonly called Hedin-vertices) instead of four-point Green's functions, see [**hedin, krien boson exchange**] to eliminate the need of calculating the full vertex F via an inversion of the irreducible vertex $\Gamma^{[13]}$. This comes in favor of the dynamical vertex approximation which benefits from the three-leg vertex description when used with a so-called λ -correction. This is shown in a later section when the “ladder”- $D\Gamma A$ and other flavors of the dynamical vertex approximation are tackled. Since we have now assembled all necessary tools to describe the properties of correlated electrons on a lattice, let us introduce the $D\Gamma A$'s purely local predecessor: the dynamical mean-field theory (DMFT).

1.8 Dynamical mean-field theory

Dynamical mean-field theory is based on the idea that in the limit of infinite spatial dimension ($d \rightarrow \infty$), the self-energy Σ_{12}^k becomes *purely local*, i.e., $\Sigma_{\text{DMFT};12}^k = \delta_{12} \Sigma_{12}^k$ [**metzner vollhardt d to infity**], where the Kronecker delta reduces the non-local self-energy to a purely local one^[14]. The intuition behind this is that in high dimensions, an electron hops to many neighbors before returning, making non-local correlations increasingly negligible^[15]. Starting from this discovery, it was shown [**georges kotliar hubbard in**] that there is a connection between an auxiliary single-impurity Anderson model (SIAM) and the Hubbard model in infinite dimensions, which allowed for a derivation of a self-consistency cycle determining the purely local self-energy. This was crucial as people were able to solve the SIAM with existing numerical many-body algorithms, effectively solving the many-body problem in the DMFT framework. This can be done using approximate^[16] and exact^[17] methods [**held dmft**]. A modern DMFT solver — which is used in this thesis to calculate input data for the dynamical vertex approximation,

^[13]In principle, one could retrieve the full vertex as $F_r^q = [(\Gamma_r^q)^{-1} - \chi_0^q]^{-1}$. However, as shown in Ref. [**schäfer nonperturbative**], the (local) irreducible vertex Γ contains an infinite set of divergencies, hence inverting it is numerically unstable.

^[14]Due to the spatial locality of the self-energy, a Fourier transform to momentum space results in a flat dispersion of Σ_{DMFT}^k .

^[15]Indeed, one can show, that the diagrams contributing to the non-local character (i.e. between lattice sites i and j) of the self-energy are suppressed by $\frac{1}{\sqrt{Z_{ij}}}$, where Z_{ij} is the number of neighbors for a given distance $\|\mathbf{R}_i - \mathbf{R}_j\|$ from lattice site i .

^[16]e.g. self-consistent perturbation theory, iterated perturbation theory or non-crossing approximation

^[17]e.g., quantum Monte Carlo (QMC), numerical renormalization group or even exact diagonalization

more on that later — is `w2dynamics` [**wallerberger w2dyn**], a continuous-time hybridization expansion (CT-HYB) QMC solver for the SIAM.

Let us briefly outline the idea and self-consistency equations of DMFT in the following, see [**held dmft**] for a more in-depth discussion. In high spatial dimensions, the number of neighboring sites Z_{ij} grows as $Z_{ij} \sim d$. To ensure a well-defined competition between kinetic energy and Coulomb interaction, the hopping amplitudes must therefore scale as

$$t_{im,jn} \rightarrow t_{im,jn}^* = \frac{t_{im,jn}}{\sqrt{Z_{ij}}}, \quad (1.79)$$

where m, n denote source and target orbitals, respectively. Furthermore, the one-particle Green's function also has to be renormalized. It is written as

$$G_{12}^k = \left[(i\nu + \mu)\delta_{12} - \epsilon_{12}^k - \Sigma_{\text{DMFT};12}^\nu \right]^{-1}, \quad (1.80)$$

where the Fourier transforms of the hopping amplitudes ϵ_{12}^k enter the Green's function, hence it scales similarly.

Diagrammatically, DMFT includes the local contribution of all topologically inequivalent Feynman diagrams which can also be obtained via the SIAM, however only if the interaction of the SIAM Hamiltonian has the same form as the original Hubbard Hamiltonian,

$$\hat{\mathcal{H}}_{\text{AIM}} = \sum_{ab;k} \epsilon_{ab}^k \hat{c}_{k;a}^\dagger \hat{c}_{k;b} + \sum_{ab} \epsilon_{ab}^d \hat{d}_a^\dagger \hat{d}_b + \frac{1}{2} \sum_{abcd} U_{abcd} \hat{d}_a^\dagger \hat{d}_c^\dagger \hat{d}_d \hat{d}_b + \sum_{ab;k} \left[V_{ab}^k \hat{d}_a^\dagger \hat{c}_{k;b} + \text{h.c.} \right]. \quad (1.81)$$

Here, \hat{d}_a^\dagger (\hat{d}_a) creates (annihilates) an electron on the impurity, whereas the operators $\hat{c}_{k;a}^\dagger$ ($\hat{c}_{k;a}$) create (annihilate) bath — i.e., non-interacting conduction — electrons, which hybridize with the localized impurity electrons via V_{ab}^k . For a successful mapping of the Hubbard model onto the AIM, there are three distinct equations in DMFT that describe a self-consistency cycle [**held dmft**]. One starts by “guessing” a local self-energy as a starting point and then iterates through the following set of equations until convergence:

$$G_{12}^\nu = \frac{1}{V_{\text{BZ}}} \int_{\text{BZ}} d\mathbf{k} \left[(i\nu + \mu)\delta_{12} - \epsilon_{12}^k - \Sigma_{\text{DMFT};12}^\nu \right]^{-1}, \quad (1.82a)$$

$$\mathcal{G}_{0;12}^\nu = \left[\left(G_{12}^\nu \right)^{-1} + \Sigma_{\text{DMFT};12}^\nu \right]^{-1}, \quad (1.82b)$$

$$G_{12}^\nu = \langle \mathcal{T} \hat{d}_1 \hat{d}_2^\dagger \rangle \quad \text{and} \quad (1.82c)$$

$$\Sigma_{\text{DMFT};12}^\nu = \left(\mathcal{G}_{0;12}^\nu \right)^{-1} - \left(G_{12}^\nu \right)^{-1}. \quad (1.82d)$$

Here, $\mathcal{G}_{0;12}^\nu$ denotes the local and non-interacting propagator of the impurity. The numerically challenging part is the computation of the AIM's Green's function in Eq. (1.82c) for which a number of different solvers are available, see the beginning of Sec. 1.8.

1.9 Dynamical vertex approximation

DMFT — as a local framework — is very capable of describing strong quasiparticle renormalization and the Mott-Hubbard metal-to-insulator transition in heavy fermion systems and transition metal

oxides accurately. Its capabilities extend way beyond that, where successful descriptions of (anti-)ferromagnetic structure effects including metamagnetism, influence on ferromagnetic properties through the lattice and Hund’s coupling, scattering at spins or impurities and many more have been reported [**held dmft**]. As wide as the range of DMFT’s capabilities extends, it still comes with a major drawback: the exclusion of non-local correlations. Numerous scientific phenomena, including the formation of valence bonds, pseudogaps, and d-wave superconductivity, as well as (para-)magnons, quantum critical behavior, and generally the critical behavior in the proximity of phase transitions, are caused by such non-local correlations.

There are two main routes to extend DMFT beyond the local scope to also include non-local correlations [**rohringer two particle**] (i) cluster extensions and (ii) diagrammatic extensions. Cluster extensions make use of a small cluster of impurities that are embedded in a bath of non-interacting conduction electrons. Non-local interaction effects within this cluster are then taken into account, making it possible to capture short-range fluctuations. Diagrammatic extensions on the other hand extend DMFT by explicitly adding non-local diagrammatic contributions. The dynamical vertex approximation falls into the latter one and will be in the main focus of this thesis, more specifically the self-consistent “ladder” variant [**josef sc dga**]. For other flavors of D Γ A, we refer the reader to Refs. [**del re, valli nanorings, schäfer multimethod, kat.tos.held 2009**], which are all excellent reads. For a first introduction to the “standard” description of the dynamical vertex approximation, we refer the reader to Ref. [**kat.tos.held 2007**]. We will extend the existing description by including the purely non-local Coulomb interaction to the irreducible vertex and follow the derivation outlined in Ref. [**ab initio dga**] closely.

The D Γ A uses a converged DMFT solution, thus including all local diagrams. It then solves the Schwinger-Dyson equation (1.77) using an approximated (full) vertex. We will show the “ladder”-approach, which reduces the numerical complexity by assuming locality of the pp-(ir-)reducible diagrams^[18]. For the following, we assume that we already have an existing converged DMFT solution at hand, containing all local diagrams. The quantities we require for the execution of the dynamical vertex approximation are the DMFT self-energy, the local two-particle Green’s function and the local irreducible vertex in the particle-hole channel^[19].

At the heart of D Γ A is the irreducible vertex in the particle-hole channel^[20], which we extend by the purely non-local Coulomb interaction,

$$\Gamma_{1234;\sigma\sigma'}^{\mathbf{q}\mathbf{k}\mathbf{k}'} = \Gamma_{1234;\sigma\sigma'}^{\omega\mathbf{v}\mathbf{v}'} + \mathcal{V}_{1234;\sigma\sigma'}^{\mathbf{q}\mathbf{k}\mathbf{k}'}, \quad (1.83)$$

where $\mathcal{V}_{1234;\sigma\sigma'}^{\mathbf{q}\mathbf{k}\mathbf{k}'}$ is given by the crossing-symmetric expression (similar to Eq. (1.48))

$$\mathcal{V}_{1234;\sigma\sigma'}^{\mathbf{q}\mathbf{k}\mathbf{k}'} = \frac{1}{\beta^2} \left[V_{1234}^{\mathbf{q}} - \delta_{\sigma\sigma'} V_{1432}^{\mathbf{k}'-\mathbf{k}} \right]. \quad (1.84)$$

This vertex can now be seen as containing all local irreducible diagrams plus the non-locality of the first order, providing a natural extension to this framework. This means that we have now included the first-order term — which is also the major contributor to the irreducible vertex — fully momentum-dependent. We will, similar to Ref. [**ab initio dga**], exclude from now on the transversal particle-hole

^[18]This is not a priori justified, however, results of the full (parquet) D Γ A equations yield a negligible contribution of the particle-particle channel to the full vertex F in the presence of strong spin fluctuations close to the antiferromagnetic phase transition in two dimensions [**kat.tos.held 2008**]. It is therefore reasonable to neglect the non-locality of the particle-particle channel diagrams. For superconducting properties on the other hand, these non-local diagrams are quite essential.

^[19]For the asymptotics of the vertex functions as described in Sec. 1.5, we also require the local two-particle Green’s function in the pp-channel.

^[20]From now on, if not explicitly specified otherwise, we will always assume the frequency notation and channel reducibility to be particle-hole like.

contribution to the non-local irreducible vertex in Eq. (1.83), similar to the GW approach [GW tomczak], which will reduce the complexity of the D Γ A equations considerably, since two out of three momentum indices vanish; the only leftover one from now on is the transfer momentum \mathbf{q} . This yields for the irreducible vertex in ph-channel for the d/m spin combinations

$$\Gamma_{d;1234}^{qv v'} = \Gamma_{d;1234}^{\omega v v'} + \frac{2}{\beta^2} V_{1234}^q \quad \text{and} \quad (1.85a)$$

$$\Gamma_{m;1234}^{qv v'} = \Gamma_{m;1234}^{\omega v v'}. \quad (1.85b)$$

From this, the Bethe-Salpeter equation in the ph-channel of Eq. (1.64) reduces to

$$F_{d/m;1234}^{qv v'} = \Gamma_{d/m;1234}^{qv v'} + \sum_{abc\partial;v_1} \Gamma_{d/m;12ab}^{qv v_1} \chi_{0;ba\partial c}^{qv_1 v_1} F_{d/m;c\partial 34}^{qv_1 v'}, \quad (1.86)$$

where

$$\chi_{0;abc\partial}^{qv v'} = \sum_{kk'} \chi_{0;abc\partial}^{qkk'} = -\beta \sum_{kk'} G_{a\partial}^k G_{cb}^{k'-q}. \quad (1.87)$$

From now on we will sometimes work with grouped indices, as described at the end of 1.6, to simplify the following derivation of the D Γ A equations. Notice that the grouped indices are now $\{n_1, n_2, v\}$ and $\{n_3, n_4, v'\}$, respectively, and do not include any momenta anymore. We will denote quantities written in grouped indices as bold quantities, similar to before. We can now see that the numerical implementation of the D Γ A equations is easier, since the vertex matrices decrease in size from $(N_k \cdot N_v \cdot N_{\text{bands}}^2) \times (N_k \cdot N_v \cdot N_{\text{bands}}^2) \rightarrow (N_v \cdot N_{\text{bands}}^2) \times (N_v \cdot N_{\text{bands}}^2)$, which reduces the storage capacity by N_k^2 and the number of operations by N_k^2 for matrix multiplication and N_k^3 for matrix inversion compared to the full parquet approach.

In principle, it would be straightforward to retrieve the full vertex via $\mathbf{F}_r^q = [(\mathbf{F}_r^q)^{-1} - \chi_0^q]^{-1}$ from Eq. (1.71). This poses numerical problems, as already stated at the end of Sec. 1.7. Thus, we aim to rewrite the inversion of the irreducible vertex \mathbf{F} using the local variant of Eq. (1.64) and Eq. (1.85),

$$\mathbf{F}_d^q = \frac{\mathbf{F}_d^\omega}{\mathbb{1} + \chi_0^\omega \mathbf{F}_d^\omega} + \frac{2}{\beta^2} \mathbf{V}^q \quad \text{and} \quad (1.88a)$$

$$\mathbf{F}_m^q = \frac{\mathbf{F}_m^\omega}{\mathbb{1} + \chi_0^\omega \mathbf{F}_m^\omega}, \quad (1.88b)$$

where $\mathbb{1}$ is an identity matrix in grouped index space. After some algebra, the full vertex in the density and magnetic spin combination read

$$\mathbf{F}_d^q = \left[\mathbf{F}_d^\omega + \frac{2}{\beta} \mathbf{V}^q (1 + \chi_0^{nl;\omega} \mathbf{F}_d^\omega) \right] \left[\mathbb{1} - \chi_0^{nl;q} \mathbf{F}_d^\omega - \frac{2}{\beta} \chi_0^q \mathbf{V}^q (1 + \chi_0^{nl;\omega} \mathbf{F}_d^\omega) \right]^{-1} \quad \text{and} \quad (1.89a)$$

$$\mathbf{F}_m^q = \mathbf{F}_m^\omega \left[\mathbb{1} - \chi_0^{nl;q} \mathbf{F}_m^\omega \right]^{-1}. \quad (1.89b)$$

Here, the purely non-local susceptibility $\chi_0^{nl;q}$ is given by

$$\chi_0^{nl;q} = \chi_0^q - \chi_0^\omega. \quad (1.90)$$

Rewriting the full vertex this way avoids the aforementioned numerical difficulties that lie in the inversion of the irreducible vertex \mathbf{F} , however we still have to deal with the inclusion of the transversal particle-hole channel, since the above equations were generated though the BSE (1.64) in the ph-channel only. The BSE only carries over the swapping symmetry of the two-particle Green's function

to the (ir-)reducible vertices Γ and Φ . The crossing symmetry of the full vertex can be restored by explicitly adding diagrams that belong to the transversal particle-hole channel. We therefore modify the parquet-decomposition in Eq. (1.33) in the following way (for $r \in \{d/m\}$)

$$F_{r,1234}^{qkk'} = F_{r,1234}^{\omega vv'} + V_{r,1234}^q + \left(\Phi_{r,1234}^{qv v'} - \Phi_{r,1234}^{\omega vv'} \right) + \left(\Phi_{r,ph;1234}^{qkk'} - \Phi_{r,ph;1234}^{\omega vv'} \right), \quad (1.91)$$

where $V_{r,1234}^q = \frac{2}{\beta^2} \delta_{rd} V_{1234}^q$. Here, all diagrams in the pp-channel and all fully irreducible diagrams (except the bare interaction $V_{r,1234}^q$) are local. We furthermore find via the local and non-local BSE,

$$\left(\Phi_{d,1234}^{qv v'} - \Phi_{d,1234}^{\omega vv'} \right) = F_{d,1234}^{nl;qv v'} - \frac{2}{\beta^2} V_{1234}^q \quad \text{and} \quad (1.92a)$$

$$\left(\Phi_{m,1234}^{qv v'} - \Phi_{m,1234}^{\omega vv'} \right) = F_{m,1234}^{nl;qv v'}, \quad (1.92b)$$

where $F_{r,1234}^{nl;qv v'}$ is defined analogously to the purely non-local susceptibility

$$F_{r,1234}^{nl;qv v'} = F_{r,1234}^{qv v'} - F_{r,1234}^{\omega vv'}. \quad (1.93)$$

We can express the difference of the transversal particle-hole diagrams of Eq. (1.91) with the help of Eq. (1.37), yielding

$$\left(\Phi_{d,ph;1234}^{qkk'} - \Phi_{d,ph;1234}^{\omega vv'} \right) = -\frac{1}{2} F_{d,3214}^{nl;(k'-k)(v'-\omega)v'} - \frac{3}{2} F_{m,3214}^{nl;(k'-k)(v'-\omega)v'} \quad \text{and} \quad (1.94a)$$

$$\left(\Phi_{m,ph;1234}^{qkk'} - \Phi_{m,ph;1234}^{\omega vv'} \right) = -\frac{1}{2} F_{m,3214}^{nl;(k'-k)(v'-\omega)v'} + \frac{1}{2} F_{m,3214}^{nl;(k'-k)(v'-\omega)v'}. \quad (1.94b)$$

We can combine these results in Eq. (1.91) which now states

$$F_{d,1234}^{qkk'} = F_{d,1234}^{\omega vv'} + F_{d,1234}^{nl;qv v'} - \frac{1}{2} F_{d,3214}^{nl;(k'-k)(v'-\omega)v'} - \frac{3}{2} F_{m,3214}^{nl;(k'-k)(v'-\omega)v'} \quad \text{and} \quad (1.95a)$$

$$F_{m,1234}^{qkk'} = F_{m,1234}^{\omega vv'} + F_{m,1234}^{nl;qv v'} - \frac{1}{2} F_{d,3214}^{nl;(k'-k)(v'-\omega)v'} + \frac{1}{2} F_{m,3214}^{nl;(k'-k)(v'-\omega)v'}. \quad (1.95b)$$

Within the approximations introduced above, the connected part of the self-energy (see Eq. (1.77) and below) loses the momentum-dependent contribution from the non-local bare interaction $V_{1234}^{k'-k}$ and now reads

$$\Sigma_{12}^k = \Sigma_{HF;12}^k - \frac{1}{\beta} \sum_{\substack{abcdef \\ qv'}} \left[U_{abc}^q \chi_{0;cbe\delta}^{qv'v'} F_{d;\delta e2f}^{qv'v} + \frac{1}{2} \tilde{U}_{abc} \chi_{0;cbe\delta}^{qv'v'} \left[F_{d;\delta e2f}^{nl;qv'v} + 3 F_{m;\delta e2f}^{nl;qv'v} \right] \right] G_{af}^{k-q}. \quad (1.96)$$

From the purely local part of this equation (c.f. first term in the brackets of Eq. (1.96)) one can extract the DMFT self-energy, since the ph-channel contribution with the local U_{1234} can be rewritten as

$$\Sigma_{ph;U;12}^k = \Sigma_{HF;12}^k - \frac{1}{\beta} \sum_{qv'} U_{abc} \left(\chi_{0;cbe\delta}^{nl;qv'v'} + \chi_{0;cbe\delta}^{\omega vv'} \right) F_{d;\delta e2f}^{\omega vv'} G_{af}^{k-q} \quad (1.97)$$

$$= \Sigma_{DMFT;12}^v + \Sigma_{HF;12}^{nl;k} - \frac{1}{\beta} \sum_{qv'} U_{abc} \chi_{0;cbe\delta}^{nl;qv'v'} F_{d;\delta e2f}^{\omega vv'} G_{af}^{k-q}, \quad (1.98)$$

where $\Sigma_{HF;12}^{nl;k}$ is the purely non-local Hartree-Fock term with the contributions from V_{1234}^q , see Eq. (1.77). We can take advantage of the momentum and frequency structure in the SDE above to simplify the numerical calculation of the self-energy. Therefore, we — in analogy to [ab initio dga] — define three Hedin vertices

$$\gamma_{r,1234}^{\omega v} = \sum_{ab;v'} \chi_{0;12ab}^{\omega vv'} F_{r;ba34}^{\omega vv'}, \quad (1.99)$$

$$\gamma_{r,1234}^{qv} = \sum_{ab;\nu'} \chi_{0;12ab}^{nl;q\nu'\nu'} F_{r;ba34}^{\omega\nu'\nu} \quad \text{and} \quad (1.100)$$

$$\eta_{r,1234}^{qv} = \sum_{ab;\nu'} \left[\chi_{0;12ab}^{qv'\nu'} F_{r;ba34}^{qv'\nu} - \chi_{0;12ab}^{\omega\nu'\nu'} F_{r;ba34}^{\omega\nu'\nu} \right]. \quad (1.101)$$

The completely local Hedin vertex can straightforwardly be retrieved from DMFT. The vertex η_{1234}^{qv} in spin combinations d/m can be calculated efficiently with a matrix inversion

$$\eta_d^q = (\vec{\mathbb{1}} + \gamma_d^\omega) \left(\left[\mathbb{1} - \chi_0^{nl;q} F_d^\omega - \frac{2}{\beta^2} \chi_0^q V^q (\vec{\mathbb{1}} + \gamma_d^\omega) \right]^{-1} - \mathbb{1} \right) \quad \text{and} \quad (1.102a)$$

$$\eta_m^q = (\vec{\mathbb{1}} + \gamma_m^\omega) \left(\left[\mathbb{1} - \chi_0^{nl;q} F_m^\omega \right]^{-1} - \mathbb{1} \right), \quad (1.102b)$$

where $\vec{\mathbb{1}}_{1234} = \delta_{14} \delta_{23}$, contrary to $\mathbb{1}$, which is an identity in grouped indices. Combining these expressions and simplifying it [**ab initio dga**] yields the D Γ A self-energy

$$\begin{aligned} \Sigma_{D\Gamma A}^k &= \Sigma_{DMFT}^v + \Sigma_{HF}^{nl;k} - \frac{1}{\beta} \sum_q \left(U + V^q - \frac{\tilde{U}}{2} \right) \eta_d^q G^{k-q} \\ &\quad + \frac{3}{2\beta} \sum_q \tilde{U} \eta_m^q G^{k-q} - \frac{1}{\beta} \sum_q (V^q \gamma_d^\omega - U \gamma_d^q) G^{k-q}. \end{aligned} \quad (1.103)$$

1.10 Self-consistent dynamical vertex approximation

The self-energy obtained from a simple “one-shot” calculation with the dynamical vertex approximation does not (always) show the correct asymptotic behavior. This deficiency is even more pronounced for higher values of the physical susceptibilities [**sc ladder dga josef**]. In addition, the susceptibilities that can be derived from the full vertex diverge at the DMFT Néel temperature. This is concerning, since it therefore violates the Mermin-Wagner theorem [**mermin-wagner**] for the case of two-dimensional systems. This can be resolved by applying a so-called λ -correction [**moriya**], where enforcing a specific sum rule of the spin (and charge) susceptibilities yields a renormalization parameter λ , which is in turn used to renormalize physical susceptibilities in the D Γ A routine.

The formalism for the λ -correction is currently only viable in the one-band regime, a straightforward extension to multi-orbital systems has not been discovered yet. The reasons being (i) λ would become a matrix object with as many entries as spin-orbit combinations exist, yielding a multidimensional optimization problem; and (ii) the solution of this multidimensional problem can be non-unique and there is no rules of which of these solutions to choose, hence the approach using a regularization scheme with the help of a λ -correction is not suitable for multi-orbital systems, which are in the focus of this thesis. Therefore, to “repair” the violation of the Mermin-Wagner theorem, we will employ a different scheme, a so-called self-consistency iteration, more on that later.

Since the λ -correction is currently not possible for multi-band systems, simply using a non-renormalized one-shot ladder-D Γ A calculation might be a first approach. However, this comes with major drawbacks: it lacks viable descriptions in parameter regimes where non-local corrections are large [**sc ladder dga josef**], e.g., where the DMFT susceptibilities diverge due to a phase transition. The source of this is two-fold: (i) due to the assumed locality of the particle-particle reducible diagrams in the ladder-D Γ A equations, which would dampen the particle-hole fluctuations [**rohringer impact of nonlocal**], the ladder diagrams of the particle-hole channel lack non-local contributions; and (ii) the self-energy entering the Bethe-Salpeter equations would still only be the local DMFT self-energy. Hence any non-local

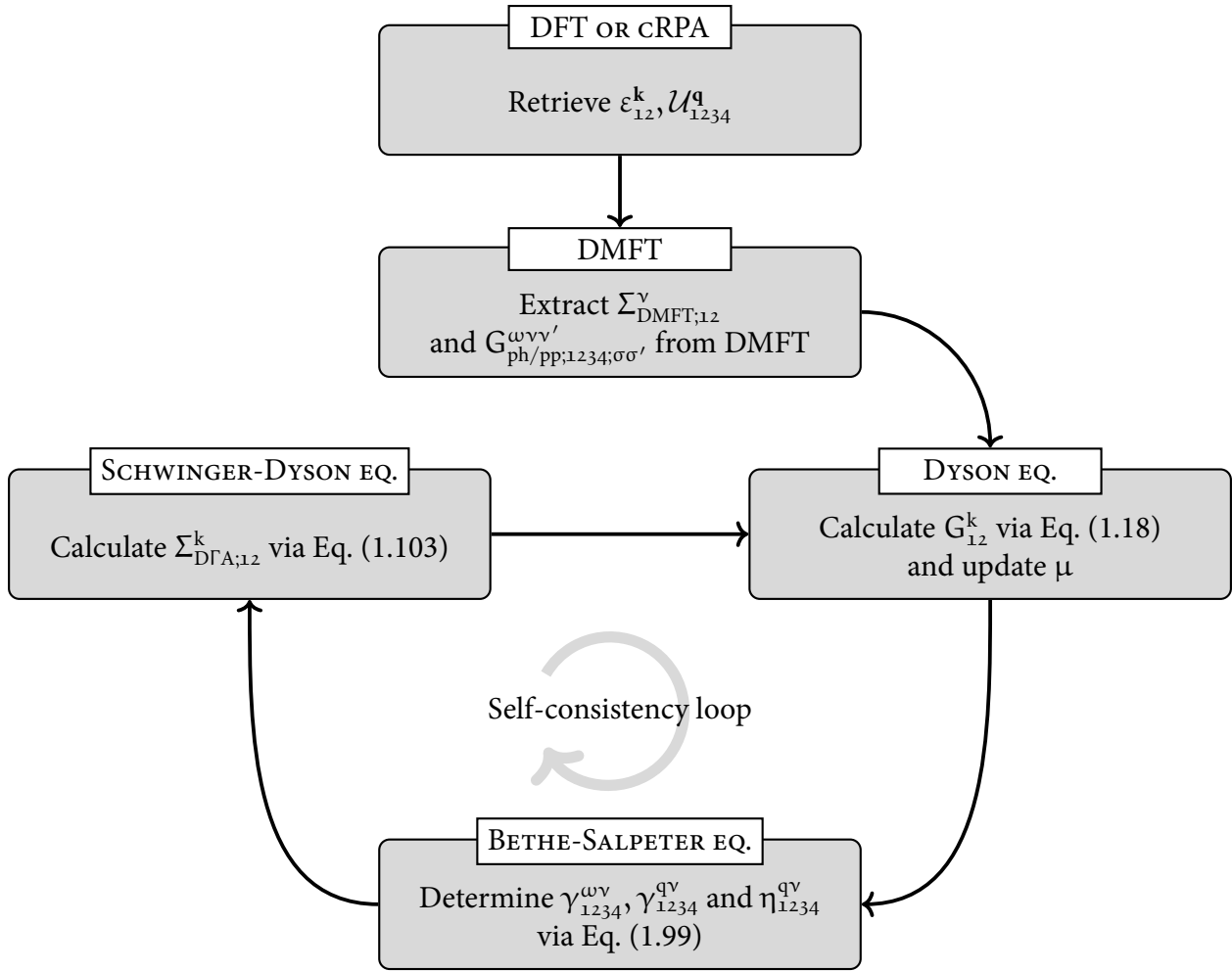


FIGURE 1.16 – This flowchart shows the D Γ A self-consistency cycle. The first box is concerned with the bandstructure and interaction calculations using DFT and/or cRPA. The next box denotes the DMFT calculation which is performed using the previously calculated quantities. From the converged DMFT calculation we extract the DMFT self-energy and local two-particle vertex functions, such as the two-particle Green’s function in the ph and pp-channel. The three boxes below describe the self-consistency cycle of the D Γ A approach. The output quantities from DFT/cRPA and DMFT (except for the chemical potential μ) are kept constant throughout the D Γ A self-consistency cycle.

contributions in that regard are simply missing. These two problems can be solved by applying a self-consistency scheme within the D Γ A equations as shown in Fig. 1.16. The steps to acquire a converged D Γ A routine with an appropriate self-energy and vertex functions are as follows:

1. First, a lot of preprocessing has to be done before the actual D Γ A equations can be iterated self-consistently. At first, it requires the calculation of the bandstructure ϵ_{12}^k and the (non-)local interaction \mathcal{U}_{1234}^q with DFT and/or cRPA. Using the momentum-dependent bandstructure and the local interaction obtained, we start a DMFT calculation with the impurity solver of choice. After the DMFT calculations are converged, the necessary local one- and two-particle quantities, such as the local self-energy and certain local vertex functions, are extracted. All of these quantities serve as the input for the following D Γ A calculation.

2. The first step in the sc-D Γ A routine is the calculation of the one-particle Green's function via the Dyson equation (1.18). This is done with the local self-energy from DMFT in the first iteration and then with the non-local self-energy calculated from the non-local SDE of the previous iteration.
3. The next step is to update the chemical potential from the newly acquired Green's function, since the eigenenergies of the particles are subject to change and the underlying Fermi-Dirac distribution needs to be adapted accordingly.
4. We then proceed with the calculation of the necessary (non-local) Hedin vertices, see Eq. (1.99). Due to the large matrices involved in the determination of $\eta_{d/m;1234}^{qv}$, it is hence the numerically most expensive step of the whole D Γ A cycle.
5. To complete the cycle, the self-energy of the current iteration is finally calculated via Eq. (1.103) using the previously acquired vertices. The self-energy then enters the Green's function again via the Dyson equation, see step 2. To ensure a steady convergence, the self-energy that enters the Green's function is mixed linearly with a parameter α , such that $\Sigma_n = \alpha\Sigma_n + (1 - \alpha)\Sigma_{n-1}$, where n denotes the iteration number and α is typically chosen around 0.2 – 0.4. Other mixing schemes, such as Periodic Pulay mixing [**pulay**], have been used previously [**my bac thesis**] without significant improvement in convergence speed and behavior, considering the additional computational and storage cost. To determine whether the self-energy is converged or not, a simple criteria comparing the magnitude of the self-energy from the previous iteration and the current iteration is used.
6. Once the dynamical vertex approximation is converged, some postprocessing steps are typically executed.